TÉCNICO LISBOA

Friction and wear behavior of femtosecond laser nanotextured metallic surfaces lubricated with graphene

Ricardo Jorge Clemente Martins

Thesis to obtain a Master of Science Degree in

Materials Engineering

Supervisor: Prof. Maria Amélia Martins de Almeida

Examination Committee

Chairperson: Prof. Maria Emília de Encarnação Rosa

Supervisor: Prof. Maria Amélia Martins de Almeida

Mermber of the Committee: Prof. João Carlos Salvador Santos Fernandes

October 2020

[Page intentionally left blank]

Acknowledgments

I want to express my gratitude and appreciation to my supervisor, Professor Maria Amélia Martins de Almeida, whose guidance, support, and knowledge have been invaluable to complete my master dissertation.

To Isabel Alves and Doctor Vitor Manuel Barbas Oliveira, that taught me the necessary skills about the laser software, which allowed me to obtain the best LIPSS possible.

I want to acknowledge the researcher from IPFN - Instituto de Plasmas e Fusão Nuclear, that works on the project PEGASUS - Plasma Enables and Graphene Allowed Synthesis of Unique nanoStructures for synthesizing the graphene powder that I used in this work.

I would like to thank the following people without whom I would have not been able to complete and made it through my master's degree.

I am thankful to IST - Instituto Superior Técnico and all its staff for all the guidance and encouragement.

To my parents, brother, and family, I am indebted for everything I have in life. I am thankful for both the confidence and unconditional support you have selflessly given me in my life, especially in this very intense academic journey, providing me the best tools to have a successful career.

To my friends in IST, Francisco Antão and João Francisco, and to my friends from previous institutions, Rodrigo Aleixo, Patricia Prates, and João Madeira, I want to transmit my utmost gratitude for all the companionship and friendship shared along these years and for every advice and time spent helping me to make my life the monumental success it is.

Without you all, this work wouldn't have been possible

Abstract

This work is focused on studying the friction effect on the textured surface with LIPSS (“Laser-induced Periodic Surface Structures”), coated with solid lubricant, graphene oxide (GO) and graphene (Gr). Also serves to provide a better understanding of the friction behavior of tool steel surfaces with graphene-based lubricants.

The surface texturing of the steel was performed with a femtosecond laser that has a wavelength of 1024 nm and gaussian distribution. Tribological tests were carried out in a sphere-on-plane configuration, with alternating linear sliding movement.

Samples were textured with LIPSS, the orientation attained was perpendicular to the polarization direction of the laser beam. We measure and obtain an average period of 1,4 µm between grooves, MPD - Mean Profile Depth of 0,202 µm and a Ra =0,223 µm

In samples with LIPSS, with and without lubricant, tests were performed in perpendicular and parallel direction to the LIPSS and later analyzed the surfaces by scanning electron microscopy (SEM).

Comparing polished with the texturized surface, we observe a reduction in friction coefficients. Furthermore, introducing GO or GR as a coating on a polished surface, we see a higher reduction in friction coefficient, been the highest reduction attained in Gr coated surface.

Looking at the friction coefficient on a surface with LIPSS coated with GO or GR, we also have a reduction in COF and observe a reduction on LIPSS coated with graphene and parallel alignment.

Keywords: LIPSS textures; Graphene Oxide (GO); Graphene (Gr); Tribology

Resumo

Este trabalho tem como objetivo estudar o efeito do atrito na superfície texturizada com LIPSS (Laser-induced Periodic Surface Structures), revestido com lubrificantes sólidos: óxido de grafeno (GO) e grafeno (Gr). Também serve para fornecer uma melhor compreensão do comportamento de atrito de superfícies de aço ferramenta com lubrificantes à base de grafeno.

A texturização da superfície do aço foi realizada com laser de femtosegundo com comprimento de onda de 1024 nm e distribuição gaussiana. Os testes tribológicos foram realizados na configuração esfera no plano, com movimento de deslizamento linear alternado.

As amostras foram texturizadas com LIPSS, a orientação obtida foi perpendicular à direção de polarização do feixe de laser. Medimos e obtemos um período médio de 1.4 µm entre ranhuras, MPD - Profundidade Média do Perfil de 0,202 µm e um Ra = 0,223 µm

Nas amostras com LIPSS, com e sem lubrificante, os testes foram realizados nas direções perpendicular e paralela à orientação dos LIPSS e posteriormente analisadas as superfícies por microscopia eletrónica de varrimento (MEV).

Comparando a superfície polida com a texturizada, observamos uma redução nos coeficientes de atrito. Além disso, introduzindo GO ou GR como um revestimento em uma superfície polida, vemos uma maior redução no coeficiente de atrito, sendo a maior redução alcançada na superfície revestida com Gr.

Olhando para o coeficiente de atrito em uma superfície com LIPSS revestida com GO ou GR, também temos uma redução no COF e observamos a redução em LIPSS revestida com grafeno e alinhamento paralelo.

Palavras-chave: Óxido de grafeno (GO); Grafeno (Gr), LIPSS, Tribologia.

Summary

List of Figures and Tables

Figures

Tables

List of Acronyms

LIPSS – Laser-Induced Periodic Surface Structures.

GO – Graphene Oxide

Gr – Graphene

HAZ – Heat Affected Zones

EDS – Energy Dispersive Spectroscopy

FS – Femtosecond

SEM – Scanning Electron Microscopy

BSE -Backscattered electrons

COF – Coefficient of friction

CA- Contact angle

rGO - Reduced graphene oxide

ANSI - American National Standards Institute

ISO - International Standardization Organization

PTFE - Polytetrafluoroethylene

IPFN – Instituto de Plasma e Fusão Nuclear

PEGASUS – Plasma Enables and Graphene Allowed Synthesis of Unique nanoStructures

[Page intentionally left blank]

1. Introduction

Although tribological concepts are much older than its industry, it has always been connected to industrial problems since their birth. Tribology establishes relationships between phenomena such as friction, wear, and lubrication for different types of mechanical contacts. These types of studies are necessary to ensure the safety and performance of any equipment.

Tribology produces knowledge to study principles and foundations linked to the contact of bodies, investigates, and offers a better understanding of chemical and physical surface treatments such as LIPSS - Laser Induced Periodic Surface Structures. This past decade there has been an increase in studies that show the different performance between modified surfaces, laser-induced periodic structures, or LIPSS in new materials while using new lubricants.

With fast grow for new, better, more complex technological advances in industrial machinery: aerospace (planes/rockets), manufacturing (equipment's for production), and automotive (car/trucks/trains), other complementary (but no less vital) industries, such as lubricant industry has been eclipsed or pushed to research laboratory advances.

As stated in 2018[1], concepts like tribology are described in numerous papers: nevertheless, it is still unknown or has relatively low visibility among both the engineering field and the general public despite its essential role to the industrial world as well as to the everyday life. As this science sprouts notoriety, hopefully, new researches in related areas can yield a “golden age” of tribology in the coming years.[1]

With the necessity for better-quality or specific lubricants: lubricants with longer lifetimes, less friction (less wear), more environmentally friendly or that could be applied in distinct fields/industries that command a considerable amount of capital opening the door for new studies or new lubricants both, solid and liquid. The development and discovery of new materials like graphene that fills all the requirements mentioned above support the creation of this work.

As stated before, we investigate two vital friction reduction mechanics, one is surface enhancement, manipulating the formation of laser-Induced Periodic Surfaces Structures (LIPSS) can decrease the real contact area thus improving friction and wear. The other is to see if LIPSS could work as lubricant reservoirs.

LIPSS is a phenomenon where there is a change in the surface topography by means of laser radiation. This technology has been increasingly used in providing color for technical surfaces[2], the control of surface wetting,[3] the tailoring of surface colonization by bacterial biofilms,[4] and the improvement of the tribological performance of nanostructured metal surfaces[5]. LIPSS can take different forms and shapes, which means it requires a profound analysis for each application.

We will focus our efforts on designing the LIPPS for three vital roles in friction and wear reduction: reduce the real contact area (lower adhesion and lower friction), entrapment of wear particles, and finally act as a lubricant reservoir.

One of the most vital and used technologies in manufacturing industries is laser technology. A combination between (I) high-speed manufacture; (II) excellent control of the shape and size of the patterns; (III) ability to reduced material waste; and (IV) ability to create complex parts or segments, making this type of equipment, without a doubt, a wonder of the twenty-first century.

We chose femtosecond laser for this work because of its unique capability to use an ultrashort pulse width, an electromagnetic pulse whose time duration is of the order of 10^{-15} seconds, and ultrahigh peak power that can safely process almost all material. Since FS laser is ideal to be used in surface texturing for tribological applications because it provides us with exceptional control, we expect to minimize the melt ejection and heat-affected zones (HAZ).

After the discovery of 2D materials, especially graphene, a carbon-based material, a new light was shined in the lubricant industry. With this in mind, we decided to study the influence that graphene-based solid lubricant has on LIPSS tribological properties.[6]

1.1. Motivation

My motivation for this work is that there are many open questions remaining, concerning fields like tribology for new materials. So, creating knowledge, developing, testing, and validating new techniques/methods are the most critical aspects for a materials engineering student like me.

The second is the necessity of reducing energy loss in several industries. Kenneth Holmberg and Ali Erdemir [7][8] stated that in total, ~23% (119 EJ) of the world's total energy consumption originates from tribological contacts. Where 20% is for overcoming friction, 3% is to remanufacture worn parts and spare equipment due to wear and wear-related failures. Also, establish that 30% of the energy in transport is to overcome friction while in the industry is about 15 – 20%. In residential and other areas, the power to overcome friction is less than 10%.

With this in mind, understanding what happens at macro, micro, and nanoscale is essential and has an enormous impact on machinery reliability and performance. Thus, creating a great market and a strong request for machines that use less energy with the same output, in addition to having a better service life for the same components. Achieving such results could only be done by the development of new materials or lubricants. All this can correspond to less money invested in repairing and designing parts.

Since we are using lubricants in our work, it is necessary to have some information about the global lubricants market. The focus of solid/dry lubricants is currently on the Chinese market, which has been the largest consumer of solid/dry lubricants due to its growing automotive industry. The automotive sector has been the primary market for these lubricants for many years because it is applied in greases-based products for lubrication systems such as ball joints, wheel bearing, etc.

Fast industrial advances for new materials like aluminum, metal alloys, and composites, creates high demand, with the objective to minimize inertia, weight, friction, resistance to wear and heat. Granting a considerable opportunity to conceive specialized/engineered lubricants, like a graphene-based lubricant, to solve the problems of rust, wear, friction associated with materials, and to apply in specific environments and industries.[9]

Finally, the oil-based lubricant market is supposed to increase from 157.6 billion USD in 2020 to 180 billion by 2025.[9] According to Grand view research, the global lubricants market size will reach USD 167.5 billion by 2027.[10] According to Infoholic Research, the graphite lubricant market will be around $1.67 billion by 2022.[11]

1.2. Objectives

The objective of this work is to study and improve the tribological behavior of tool steel surfaces textured by laser, with graphene-based lubricant. Also, understanding if LIPSS can act as a reservoir. The study focuses on tribological tests at the nanoscale on texturized tool steel surfaces.

The tests done on tool steel samples with three surface finishes: (i) polished, (ii) laser textured surface, and (iii) polished and textured coated surfaces with graphene oxide (GO) or graphene (Gr).

The tribological tests use a sphere-on-plane configuration, with an alternating linear sliding motion. In the samples textured by the laser, the tests were carried out both parallel and perpendicular directions to the LIPSS. The tests allow us to measure the friction coefficient under different conditions, and the surfaces were analyzed by scanning electron microscopy to identify the material removal mechanisms.

2. State of the Art

2.1. Contact mechanics

2.1.1. Contact between solid surfaces

Contact mechanics is the study of the deformation of two bodies based on assumptions of ideal surface, shapes because real surface topography and materials are difficult to characterize. It is fundamental to understand topics like topography, Elastic and Plastic contact, hardness, friction, and wear in ideal and real circumstances.[12]

A material exhibits small irregularities on the surface even after polishing to the highest level where they can be narrowed or raised. This roughness phenomenon observed in figure 1 results in applying a load

that will lead to interaction between asperities leading to elastic or plastic deformation that increases the contact area and friction.[12]

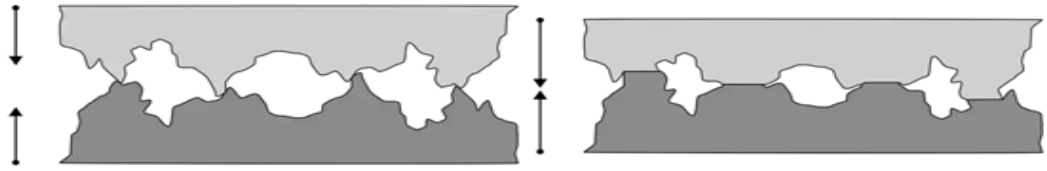

Figure 1 - Representation of surface roughness. Image reproduced from[12]

Organizations such as the American National Standards Institute (ANSI) and the International Standardization Organization (ISO) used some statistical height descriptors, to characterize the roughness:[12]

R_a, (arithmetic average); $$R_a = \frac{1}{L}\int_0^L |z(x)|dx \quad (1)$$

R_q or root mean square $$R_q^2 = \frac{1}{L}\int_0^L z^2(x)\,dx \quad (2)$$

skewness (Sk); $$S_k = \frac{1}{R_q^3}\int_{-\infty}^{+\infty} z^3 p(x)\,dx \quad (3)$$

kurtosis (K); $$K = \frac{1}{R_q^4}\int_{-\infty}^{+\infty} z^4 p(x)\,dx \quad (4)$$

2.1.2. Hertzian Contact

Contact mechanics is associated with Hertzian contact, which answers the enigma of mating two elastic bodies with curved surfaces with different radii of curvature. They will initially touch at either a point or along a line, and with the application of the smallest load, elastic deformation expands. The first analysis of this situation was presented by Heinrich Hertz in 1881 and based on the following assumptions:[12]

- The surfaces are continuous, smooth, nonconforming and frictionless.
- The size of the contact area is small compared to the size of the bodies, i.e., the strains associated with the deformations are small.
- Each solid can behave as an elastic half-space in the vicinity of the contact zone.

- ❖ The gap h between the undeformed surfaces can be approximated by an expression of the form Hertzian Contacts.

This classical solution provides a foundation for modern problems in contact mechanics, in engineering fields, and specially used in tribology.

2.1.3. Elastic contact

Following Hertzian contact, it is possible to obtain the elastic contact between two surfaces, when the normal force applied is sufficiently lower than the elastic limit of the materials is not exceeded. For example, when a sphere of radius R enters into contact with a plane under a normal force, Fn, the connection occurs in a circular area of radius a given by the equation:[12]

$$A = \pi a^2 = \pi \left(\frac{(3FnR)}{4E*} \right)^{\frac{2}{3}} \quad (5)$$

where a is the radius of the circle contact area given by.

$$a = \left(\frac{3FnR}{4E} \right)^{\frac{1}{3}} \quad (6)$$

And where the contact Module his given by E *, where the modulus of young and v is the Poisson coefficient.[12]

$$\frac{1}{E^*} = \frac{1 - v_1^2}{E_1} + \frac{1 - v_2^2}{E_2} \quad (7)$$

where E1 and E2 are Young's modulus, and v1 and v2 are the Poisson coefficients of the sphere and plane materials. R the radius of contact curvature is related to the formula (7).[12]

$$\frac{1}{R} = \frac{1}{R_1} + \frac{1}{R_2} \quad (8)$$

The radial pressure distribution on the contact surface is elliptical and has a maximum at the center of the contact area, given by equation (9) while P_0 is the average pressure and is given in equation (10).[12]

$$P_{max} = \frac{3Fn}{2\pi a^2} = \left(\frac{6FnE^{*2}}{\pi^3 R^2} \right)^{\frac{1}{3}} \quad (9)$$

$$P_0 = \frac{3}{2} P_m = \frac{3}{2} \left(\frac{6FnE^{*2}}{\pi^3 R^2} \right)^{\frac{1}{3}} \quad (10)$$

2.1.4. Plastic contact

Plastic models characterize plastic deformation, contrary to elastic contact deformation. Initially, the elastic strains of the surrounding material limit the plastic strain. The region in which plastic flow occurs is small and is surrounded by elastically flow deformation. If there is an increment in load, the area of plastic deformation spreads until it finally reaches the free surface where the maximum contact pressure is equal to 1.67 Y.[13]

At this point, plastic deformation of one of the bodies may rise, the mean pressure over the contact area has surged by this stage to about 3Y, as shown in figure 2, and remains at nearly the same value for subsequent increases in load.[13]

Once the yield criteria are satisfied the plastic flow will occur at that point. The shear stresses are maximal when the Tresca criterion is applicable (an approximation for many ductile metals which also affords arithmetical simplicity over the von Mises yield criterion), maximum shear stress of Y/2 is reached.[12][13]

$$\tau_{max} = \frac{1}{2}(\sigma_1 - \sigma_3) = \tau_{crit} = \frac{Y}{2} \tag{11}$$

where Y is the uniaxial yield stress of the material, $\sigma 1$ $\sigma 2$ and $\sigma 3$ are the principal tensions and $\sigma 1 > \sigma 2 > \sigma 3$ and $Tcrit$ is critical shear strength, and Y is the yield stress.[12]

τmax represents the maximum contact pressure value, for spherical point contact (on a material with v =0.3), the maximum shear stress of 0,31$p0$, where plastic deformation starts.

$$\tau_{max} = 0.31 p_0 = 1.6Y \tag{12}$$

$$\bar{p} = 1.1Y \tag{13}$$

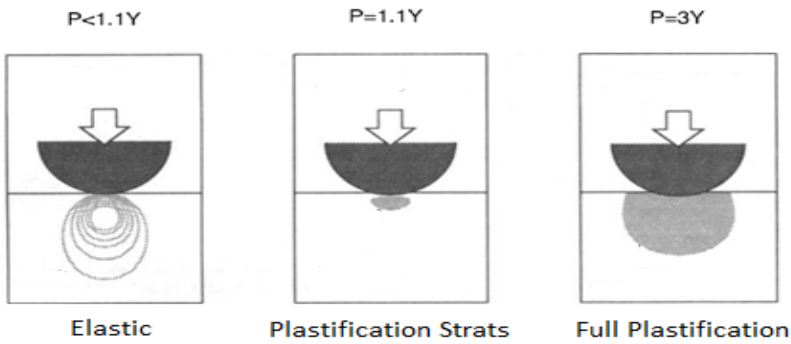

Figure 2 - Evolution of plastic deformation of a material. Image adapted from [25]

$$\begin{cases} Elastic\ deformation: A \propto F^{\frac{2}{3}} \\ Plastic\ deformation: A \propto F \end{cases}$$

2.1.5. Contact area

Roughness is a component of surface texture and requires an intensive analysis because it´s a very complex subject due to a variety of flaws/irregularities, protrusions ranging from distortions of the part, macro-scale (waviness), to micro-scale (asperities) as is displayed in figure 3.[5][12]

A good understanding of contact mechanics, adhesion, friction, and wear between the real surface topography require knowledge of the area of contact between the bodies. As such, it is crucial to produce a respectable study on wear and tear. [5][12]

Surface roughness supports the applied load acting as a limit to the small contact zones among the roughness of the surface. As previously stated, two bodies in contact exhibit a contact area. With the increase in load, the bodies approach each other, the number of contact points increases, causing the elastic and then plastic deformation of the asperities to achieve this way a new contact area. [5][12]

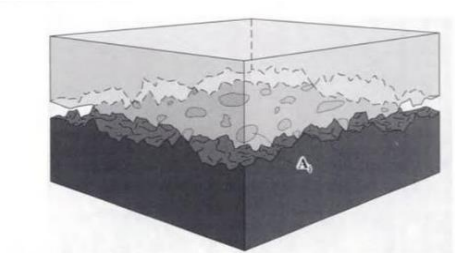

Figure 3 - Representation of surface area. Image adapted from[12]

One way to calculate the true contact area is to use statistical methods of topographic analysis of surfaces like the Abbot-Firestone curve, figure 4, as a means of representing a surface profile. The Abbott-Firestone or bearing area curve (BAC), equation 14, gives the cumulative probability distribution function of the surface profile height and can be calculated by integrating the profile trace. It allows estimating the actual contact area between a rigid fat body and a non-rigid rough body. [5][12]

The ordinates axis has the height of the roughness, the abscissa axis, we have the relative area of support, which is the percentage of the true of apparent contact that effectively supports the applied load[12].

$$P(z) = Prob(z \geq h) = \int_{h}^{+\infty} p(z)dz \tag{14}$$

Where P(z) is the probability distribution function of Z and p(z) is the probability density function of Z.

For a Gaussian (normal) distribution:

$$p(z) = \frac{1}{\sigma\sqrt{2\pi}} \exp\left(-\frac{z^2}{2\sigma^2}\right) \tag{15}$$

The actual contact area is[12]:

$$A(H) = A_n Prob(z \geq h) = A_n \int_h^{+\infty} p(z)dz = A_n[1 - P(h)] \quad (16)$$

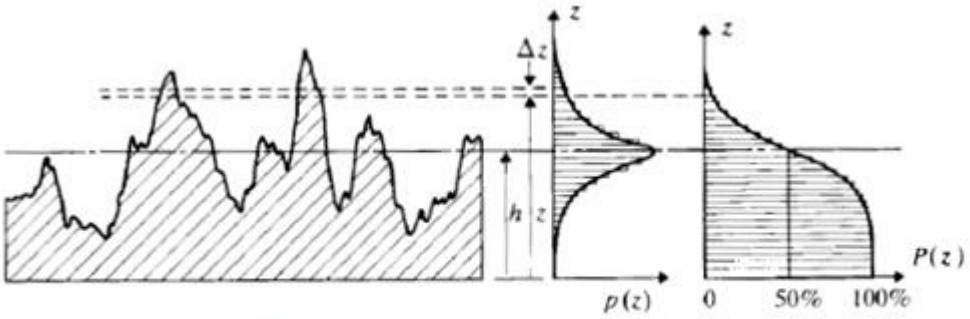

Figure 4 - Abbot-Firestone curve representation from a superficial topographic profile. (a) Surface topography, (b) Graph p (y), corresponds to the amplitude density function and represents the distribution of surface heights, (c) Abbot-Firestone curve.

2.2. Friction

Friction is a phenomenon of the resistive force present throughout the relative motion of surfaces and material elements sliding against each other. The friction coefficient $\boldsymbol{\mu}$, represented in equation 17, is a value that displays the relationship between the tangential force $\boldsymbol{F_t}$ and normal force $\boldsymbol{F_n}$ between two entities.[14]

$$\mu = \frac{F_t}{F_n} \quad (17)$$

There are two types of friction: **static** and **kinetic**

Static friction is friction exerted between two or more solid objects that are not moving relative to each other. **Kinetic friction**, also known as **dynamic friction**, occurs when two bodies are moving parallel to each other.[14]

Put it in simple terms, **static friction** is the energy that is necessary to be applied to induce movement in a body, a force that keeps a body at rest, **and kinetic friction** is a force that acts between moving surfaces. A body in motion will experience a force in the opposite direction as it progresses on the track.[12][13]

We can divide them into two classes: **Sliding** and **Rolling.** The distinction between sliding and rolling friction is useful, but the two are not mutually exclusive, and even in 'pure' rolling, there is the presence of some sliding.[13]

Using the identical conditions of sliding and in the absence of lubrication, **μ** for a given pair of materials may remain almost constant as the normal load and apparent area of contact is varied. This observation led to the formulation of **Amonton's Laws of Friction.**[13]

1. The friction force is proportional to the normal load.

2. The friction force is independent of the apparent area of contact.

3. The friction force is independent of the sliding velocity.

The first two Laws of Friction are often reliable. Most metals and numerous other materials obey them, even when exposed to a lubricated or unlubricated environment, providing a realistic approximation to what is observed, at least for macroscopic contact areas. Nonetheless, there is one exception. Polymers and other materials with a very low elastic modulus often do not obey these laws.[13]

The Third Law of Friction also has an exception, only after sliding is verified, μd is for the majority of systems nearly independent of sliding velocity, despite that for metals at high sliding speeds, [10-100] m/s μd falls with increasing velocity.[13]

When speaking about friction and trying to describe this aspect with emphasis on the tribological point of view, it is essential to have a great understanding of which factors influence friction coefficients. For example, force applied, material, temperature, the direction of sliding, the environmental conditions as well as measurement conditions related to the devices, thus, providing a more reliable assessment of tribometric measurement/results. On this basis, the process can be adjusted or even optimize the parameters for future test trials.[14]

2.2.1. Friction Coefficient

When analyzing tribology papers and literature, it is necessary to be skeptical when looking at friction coefficient values. In engineering terms, it is impossible to have a fixed value even if they are attractive and widely available. A range of μ values taken during tests over a wide range of sliding conditions is more realistic. A chart of friction ranges like the one in Figure 5 has little meaning since specific values of friction are not connected with specific sliding conditions. Although handbooks often publish values for dry steel at 0.2, one can measure values ranging from 0.1 to 1.4, and perhaps even higher, depending on sliding conditions.[12]

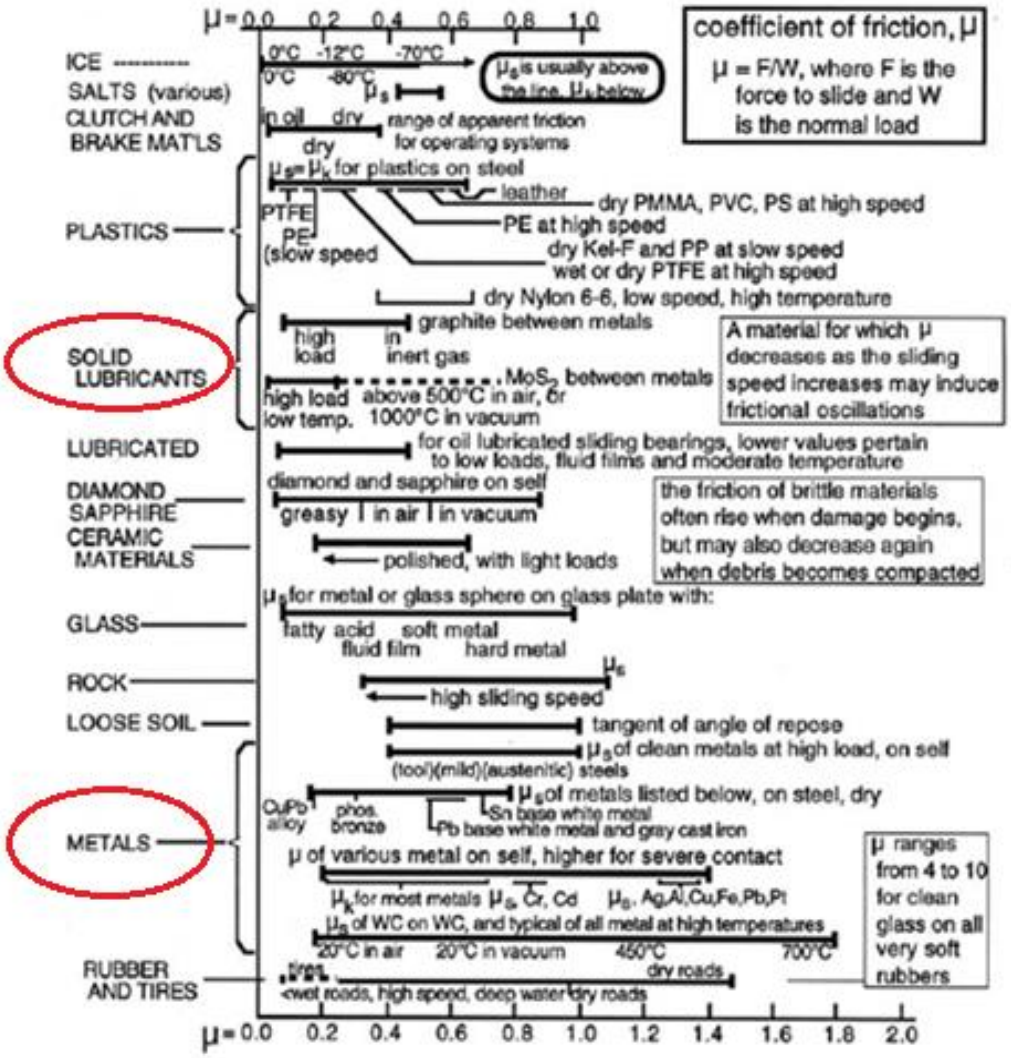

Figure 5 - A table of values of the coefficient of friction of various materials and conditions of sliding.[6]

2.2.1.1. Friction transitions during sliding

To better understand friction and wear, it is also necessary to comprehend the transitions that mating surfaces present throughout sliding, since changes in this condition affect the friction and wear properties. By looking at a typical graph produced by the tribometer, there are three stages:

I. "Run-in," "break-in," or "wearing-in" period, a phenomenon necessary for a long interface life. If not present, we will attain severe damage and early failure of the part.

II. First steady state sliding that corresponds to a stabilization in friction force,

III. Transition period that is followed by another plateau, denominated steady state slide 2,

All stages lead to a S-shaped curve like the one in Figure 6 (a). This process can continue approaching more than two stages.[15]

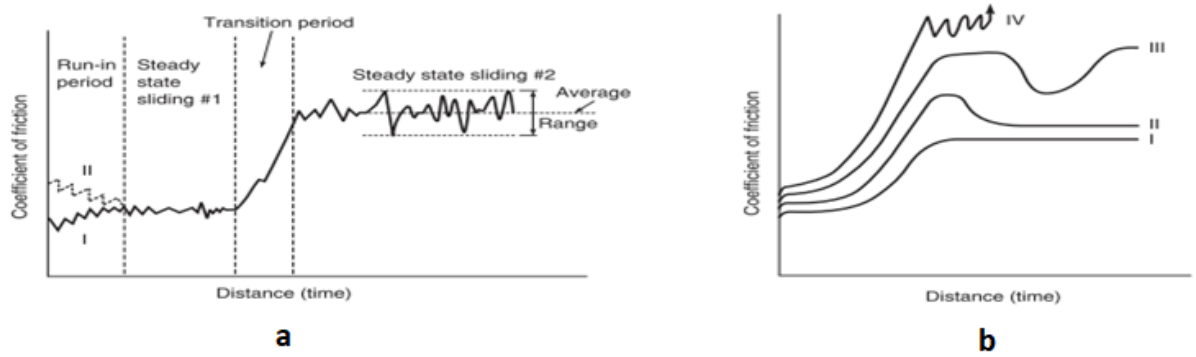

Figure 6 - Coefficient of friction as a function of sliding distance with (a) a typical S-shaped curve showing run-in period, and (b) four hypothetical cases. Adapted from [15]

During the run-in period, the high asperities will connect with another body and maybe deform causing a surge in the contact area where initial surface films may be worn out, new steady films may come into existence, or structural changes may occur. (I.e.) asperities deformation, producing an increase or decrease in friction coefficient from the initial value. After the first steady state period, changes in the interface may arise, such as roughening and trapped particles that lead to an increase in friction until we achieved another plateau.[15]

Although a friction curve retains its authenticity, lower μ in early stages passes to a higher μ to later stages with different behavior during tests. Therefore, it is necessary to have a complete analysis of what is happening in every cycle in order to understand it.[15]

The different patterns present in friction curves shown in figure 6 (b), can be described by different shapes such as:[15]

I. Friction may persist at its initial value for some time and slowly increases to another steady state value;[15]
II. After a steady state sliding period, it may first rise to a high value then level off at a lower value (but higher than the initial value); [15]
III. It may increase to a high value, level off, then the interface fails, and friction may become this value in which it failed. Then, drop to a lower plateau followed by an increase to a higher value[15]
IV. It may change in a nonrepeatable manner, figure 6. In all cases, the coefficient of friction would reach a high value after some period of sliding.[15]

In case (I) the increase in μ is associated with plowing, the roughening, and trapped wear particles leading to a larger component of adhesive friction. The drop in the friction presented in case (II) is associated with the smoothing of these two hard surfaces. The plowing factor explained in (I) is reduced

or eliminated through roughening or trapped wear particles reducing the true area of contact, which in turn reduces the adhesive component of the friction.

In case (III) the drop in friction is associated with the ejection of wear particles, followed by an increase triggered by the generation and entrapment of new wear particles. Finally, if the friction coefficient reaches an excessively high value in a brief period it means that a feeble material pair is present in which friction component is attained by all sources, case IV. [15]

2.2.2. Friction on metals

Friction in metals slide against one another has been one of the most studied subjects for tribology. Typically values, for unlubricated sliding are much lower in air environment conditions and stays in the range from 0.5 to 1.5.[13]

It is necessary to have in mind that frictional behavior also depends on factors such as the composition and microstructure of materials. One other aspect that plays a critical role in determining the sliding behavior is the presence of oxides, between surfaces or between oxide and bare metal that acts as a small layer/barrier, some exceptions may occur. The formation of oxide films often between 1 and 10 nm thickness produces a layer that lowers the friction coefficient between surfaces.[12][13]

2.2.2.1. Oxidation

There is a correlation between the destruction of the oxide film and the applied load. At low normal loads, the oxide films effectively separate the two surfaces mitigating metallic contact. Giving a low friction coefficient in most cases (but not always) lower at higher loads as a consequence, the track formed by the slider appears smooth and polished. [13][15]

With the increase of the normal load, if the oxide film is unbroken during sliding, surface damage is slight, and the oxide itself determines the coefficient of friction. However, if the oxide layer is damaged or destroyed there is a transition to a higher value of μ, the track can exhibit an indication of metallic transfer (superficial damage) and contact between asperities occurs.[13][15]

As might be expected, the wear rates associated with these two regimes are distinctly different. Nevertheless, there are some exceptions, very soft and ductile metals produce oxide films that are effortlessly punctured, due to little mechanical support, achieving a high friction coefficient with little or no change with an increase in load. [13][15]

Another extreme behavior is when a thin but sturdy oxide film is acquired, similar to the one shown in chromium surfaces, with no metallic contact that displays a constant low friction coefficient over a wide range of load. [13]

2.3. Laser-Induced Periodic Surface Structures (LIPSS)

LIPSS is the change in surface topography using laser radiation and occurs when a surface treatment creates periodic ripples/grooves in a very controllable way, figure 7.[6][5]

There are two types of LIPSS:

- "Low spatial frequency LIPSS" (LSFL) - periods near the wavelength of the radiation[6].
- "High spatial frequency LIPSS" (HSFL) - periods much lower than the radiation wavelength.[6]

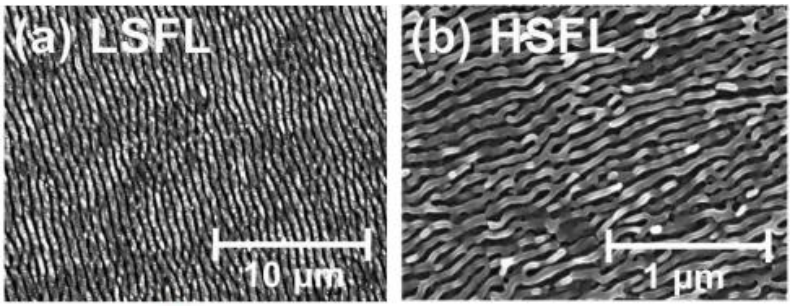

Figure 7 - SEM images of FS laser for (a) low and (b) high spatial frequency LIPSS. Image reproduced from [26].

For strong absorbing materials such as metals or semiconductors in most cases, low-spatial-frequency LIPSS (LSFL) is acquired with a period close to or somewhat smaller than the wavelength (λ) and an orientation perpendicular to the laser beam polarization.[16][17]

In dielectrics, (LSFL) observed either perpendicular or (for large bandgap materials) parallel to the beam polarization. Often, they show ripple periods either close to (λ) or close to $\frac{\lambda}{n}$, where n is the refractive index of the dielectric material[17]. High-spatial-frequency LIPSS (HSFL) with spatial periods significantly smaller than half of the irradiation wavelength have been observed predominantly for transparent materials and with orientations often perpendicular and sometimes parallel to the beam polarization.
LSFL generation is well established and accepted by the scientific community. However, a study done by Rung[18] links the formation of LSFL on steel surfaces with a surface finish. In a regime of higher surface roughness, he generated LSFL with orientation along with the linear polishing profile.

The origin of the HSFL is controversial and discussed. To this day, there is no consensus on the respective mechanisms and formation. Changing the laser processing parameters allows us to attain LIPSS, nano-waves, nano-cones, peaks, holes, columns. Frequency and type of LIPSS (HSFL or LSFL) depend on the processing parameters used, such as wavelength and incident angle of the laser beam, number of pulses and radiation fluence, laser beam polarization, environmental conditions, and material properties.[5]

2.3.1. Historical progress

In 1965 Birnbaum [19] came across a new effect after the examination of surface damage produced in semiconductors using a ruby laser. He attributed their formation to a diffraction effect and suggested that the material removal formed the surface relief.

Ever since the introduction of periodic nanoscale structures to the surface of materials, many articles were published. In 1986 Siegman [20] exhibited highly periodic, often permanent surface "ripples" on a material illuminated by a single laser beam of sufficient intensity. Yu [21] in 1999 demonstrated better tribological performance of micrometer-sized undulations in support material for magnetic data storage elements in computer hard disks (NIP).

In recent years, we have seen several advances in laser technologies. FS laser has received a higher amount of research attention and taken a crucial role due to advantages such as (I) Capability of processing non-planar surfaces; (II) ability to produce nanostructures on surface areas from microscale to macroscale; (III) processing at a high speed under normal ambient conditions, without needing a clean room environment; (IV) ability to process nearly all types of materials.[22]

Mizuno [23], and Naoki [24] investigated the tribological properties of nanostructures on a DLC film. Rosenkranz [25], and Gnilitskyi [26] confirms the importance of laser patterning on stainless steel samples. Articles done by Bonse, [27][28] provide an insight into the influence of laser radiation on titanium surfaces and titanium nitrate coatings.

In 2020 articles published by Alves [29][30] report the influence of laser surface nanotexturing on the friction behavior of the silicon/sapphire system and silicon sliding against PTFE. These are only a few of many articles that demonstrate the importance of periodic nanostructures.

2.3.2. Influence of LIPSS on tribological behavior

Surface topography plays an important role in the material tribological properties in micro and nanoscale friction behavior between two bodies during contact. Up to this day, there are different research groups around the world , solely dedicated to these phenomena to improve efficiency and increase the life span of systems or mechanical components.[31][32]

In recent years, surface nanotexturing has proven to be an emerging technique for controlling friction and wear, since reducing the area of contact will reduce the adhesion between surfaces, resulting in low friction systems.[25] [31] [33]

From an engineering point of view, the ability to enhance the tribological properties of a surface is equal to the increase of the service life of a part. Nanotexturing allows us to control tribological behavior and decrease or avoid any damaging effect on the surface.[5][31]

Tribological behavior of LIPSS is seriously affected by (I) the adhesion between the contacting bodies, (II) deformation of the asperities, and (III) surface plowing by wear particles or asperities. (a) and (b) are related to the true contact area of friction pairs, (c) is associated with surface roughness.

Alves[29], and Zhuo [34] attributed the changes in COF values to the significant contributions of plastic deformation of asperities and plowing components.

These three components of the friction coefficient must be taken into consideration when discussing these friction results. Depending on the LIPSS dimension, the contact area and alignment (perpendicular or parallel) have no difference, since the ripple structure is much smaller than the wear track.

With regards to the plowing component, when the sliding direction of the sphere sample is perpendicular to the orientation of LIPSS, the wear particles can be effectively trapped by the textured surfaces with LIPSS.

On the other hand, when the sliding direction of the ball sample is parallel, the wear debris may slide continuously with the movement of the sphere. Consequently, the average friction coefficient of perpendicular alignment is substantially lower.

Rosenkranz [25], Gnilitskyi [26], and Yu et al. [35] reported a lower COF for a perpendicular configuration where the shorter stiction length to adhesion results in a lower COF. Contradicting those findings, we have Alves[29], and Bo[36] that attain lower COF in the parallel alignment.

Therefore, a properly designed macrostructure may be extremely important, since friction properties of the laser-treated surfaces promote an increase in wear particle load capacity and wear resistance.[31]

2.3.3. Wettability

Wettability is one of the properties that can be enhanced by LIPSS. These structures can control surface hydrophobicity and can be explained by the increased roughness of the laser-treated surfaces and by the entrapment underneath the liquid, increasing the contact angle. Thus, the development of materials with optimized wettability may be relevant to applications in the biomedical field.[37]

In this section, we will focus on the wettability of our material, not for applications but has a parameter that interferes with coating deposition.

Generally, there are two opposite wetting behaviors. The first behavior defined by complete drying, in which a liquid droplet brought into contact with a solid surface remains spherical without developing any significant contact with its superhydrophobic surface that exhibits a water contact angle bigger than at least 150°.

The second is defined by complete wetting, in which a droplet brought into contact with a solid surface spontaneously spreads and forms a film super-hydrophilic that shows a water contact angle equals or near to 0°. Intermediary behaviors can also occur, in which the droplet partially wets the surface.

Therefore, it is necessary to determine which surface parameters favor these different wetting behaviors. The contact angle (CA), the angle between the tangent to the liquid surface and the surface in a point of the contact line or three phasic lines, of a liquid droplet into contact with a solid surface, defines the degree of wetting.

Another characteristic that must be taken into consideration is the different models that can apply to LIPSS: the Wenzel's, and Cassie-Baxter's model.

In the Wenzel model, the liquid comes into contact with the whole area of the rough surface, and the Cassie-Baxter's model assumes that the fluid enters into contact with substrate material and the trapped air in the roughness.

2.3.4. Laser-induced periodic surfaces structures as reservoirs.

Now we will focus on the ability of LIPSS to act as reservoirs. In 1965 Hamilton,et al. [37] and in 1998 Geige et al,.[38] showed that ceramic surfaces, treated by laser radiation, showed improved tribological properties. Ever since the first application of LIPSS on the surface for lubricant reservoirs, many researchers[31][39][40] have contributed to the fast development of this phenomenon. Bonse has taken some recognition in this area by writing some of the most cited articles[6][27][28][41][42].

In theory, using micro or nanoscale structures can serve as reservoirs, and have proven to be beneficial by controlling the flow of lubricants, reducing friction, and improve the load-carrying capacity between sliding components.

2.4. Lubricants

Lubricants can be organic or inorganic, are introduced to reduce friction between surfaces in tribological contact and have been around for a long time.

This chapter will take emphasis on some guidelines on the lubricant to better understand how solid lubricant works and which (graphene or graphene-based) could function in new technological fields.[12]

The most important thing to do when selecting a lubricant is to understand the environment in which the lubricant operates. Parameters such as temperature, environment (vacuum), presence of the reactive medium or chemical compatibility of the lubricant with the material, viscosity influence the choice lubricant, and only after considering these vital factors, one must decide what type of lubricant [12]

2.4.1. Effect of lubricants

The presence of a lubricant layer aims to reduce the shear strength of two sliding surfaces.[12] The lubricants can have the following effects: (1) Delay or suppress the first two stages of variation of the coefficient of friction; (2) Change the duration of these stages; (3) Moderate the friction and its effect on the wear rate. [12]

Figure 8 shows the behavior between two surfaces, one lubricated, and the other dry. Performances like those provide information to characterize correctly the processes that occur in the tribological system.[12]

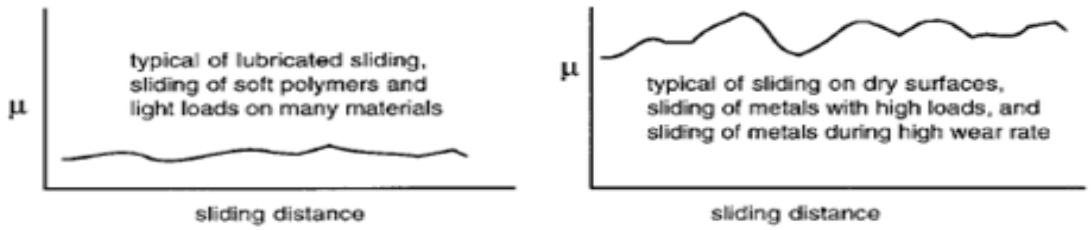

Figure 8 - Friction coefficient between two different surfaces.[13]

2.4.2. Solid Lubricants

The dry or solid lubricants are materials that, despite being in the solid phase, can reduce friction between surfaces sliding against each other without the need for a liquid oil medium.

Solid lubricants can be assorted into quite a few subclasses, classified based on the chemistry, crystal structure, and lubricity, form, or shape (i.e., thin films, powders, bulk, composite, and crystalline or amorphous states). For operations that require very high or low temperatures, vacuum, radiation, extreme contact pressure, a solid lubricant may be the only choice for controlling friction and wear.[12][43]

The solid lubricant also acts as additives, dispersed in water, oils, and greases, to attain improved friction and wear properties under conditions of extreme pressures and temperatures.[12][43] Several inorganic materials (e.g., molybdenum disulfide, graphite) can provide excellent lubrication. These solids owe their lubricity to a lamellar or layered crystal structure.

Considerable shortcomings of solid lubricants include:[12][43]

- ❖ Poor thermal conductors and, hence, cannot carry away the heat from sliding interfaces.

- Depending on the test environment and contact conditions, their friction coefficients may be high or fluctuate significantly.
- They have finite wear lives, and their replenishment is more complicated than that of liquid lubricants.
- Oxidation and aging-related degradation may occur over time and present some problems with transition-metal dichalcogenides (MX_2) with M a transition metal atom (Mo, W, etc) and X a chalcogen (S, Se or Te).
- Upon exposure to high temperatures or oxidative environments, they may undergo irreversible structural-chemistry changes that lead to loss of lubricity and the generation of some abrasive, non-lubricious by-products.

2.5. Carbon nanomaterials

Carbon is one of the most versatile elements, manifests itself in a wide variety of allotropic forms that lies in its ability to exist in three types of hybridizations, namely sp1, sp2, and sp3. These materials have been increasingly used and are attractive solid lubricants because of properties such as good corrosion resistance, excellent mechanical behaviors, and for exploring efficient ways to reduce energy consumption. The reason for that is a unique layered structure, atoms lying on the same layer are closely packed and bonded to each other with layers relatively far apart, and the forces that connect them (e.g., van der Waals) are weak. [44]

2.5.1. Graphene and graphene-based lubricants

Attributed to the availability for chemical modification, in recent years there has been a rise in research for 2D materials like graphene, a sp2-bonded two-dimensional monolayer of carbon organized in a hexagonal lattice.[45]

Graphene and the sp^2-hybridization attracted attention because of their unique and fascinating properties. For a one-atom thick material (*3.5 Å based on the interplanar spacing of crystalline graphite), it exhibits enormous high intrinsic strength of up to 130 GPa, Young's modulus of up to 1 TPa, as well as ultra-low friction.[45] [46].

Graphene´s low friction and wear properties can be attributed to the monolayer, few layers, multilayer, or reduced graphene oxide (rGO) systems that emphasize its intrinsic advantage in its ability to be used as a lubricant coating.
At the nanoscale, the friction of graphene can be affected by the sp3 functionalization of the Gr surface because fewer van der Waals contacts and larger bandgaps reduce the adhesion forces due to the

interaction between the sp2 and sp3 structures originating from their different stable volumes. [46] [47] [48]

The literature mention that one of the noticeable aspects is that graphene is the bond between p–p interactions that act as bridges to link the sheets together to form a macroscopic film.[47][48][49][50][51]

3. Experimental procedure

3.1. Materials

3.1.1. Tools steel

The steel used in this experimental work is DIN 90MnCrV8, oil-tempered, tempered cold-working tool steel with an austenitic structure and hardness of 58-60 HRc. The mechanical properties of this steel are listed below in Table 1. We converted Rockwell C hardness values to Vicker's hardness values using the Wilson conversion.[5].

Table 1 -Mechanical properties of the tool steel[5]

	Young modulus, E [GPa]	Poisson coefficient, v	Yield stress, σy [MPa]	Hardness
DIN 90MnCrV8	~200	~0,3	1750	58-60 HRc ~653-697 HV

The chemical composition of the steel DIN90MnCrV8 is listed in Table 2.

Table 2 - Chemical composition of steel DIM 90MnCrV8 by weight

C	Cr	Mn	Mo	Si	V	Ni	Cu	P	S	Fe
0,90	0,40	2,00	-	-	0,10	-	-	-	-	Bal.

3.1.2. Steel spheres

The balls used in the wear tests were from Redhill Precision Specialty Balls. Table 3 shows the characteristics and mechanical properties of steel balls.

Table 3 - Properties of steel balls used in tribological tests.[5]

Material	Diameter (mm)	wear	Young Modulus, E [GPa]	Yield strength, σy [MPa]	Poisson ratio, v	Hardness
Chromium steel AISI 52100	3	Nanowear	207	2070	0,3	60 – 66 HRc 697 – 866 HV

The spheres have higher hardness and yield strength than DIN 90MnCrV8 steel. Table 4 shows the chemical composition of these materials.

Table 4 - Chemical composition of steel ball used in tribological tests, in percentage by weight.[5]

Material	C	Cr	Mn	Mo	Si	Ni	Cu	P	S	Fe
AISI 52100	0,98-1,10	1,4-1,65	0,25-0,45	-	0,15-0,35	-	-	max 0,025	max 0,025	Bal.

3.1.3. Graphene oxide in water dispersion.

- Concentration 4mg/ml
- Monolayer content (at 0.5mg/ml) >95%
- Dispersibility
- Polar Solvent
- Particle Size:
  - D90 29 - 33 µm
  - D50 14 - 17 µm
  - D10 6 - 7 µm

Table 5 shows the chemical composition of graphene oxide (Graphenea) used in this experience.

Table 5 -Chemical composition of graphene oxide

%	C	H	N	S	O
	49-56	0-1	0-1	0-2	41-50

3.1.4. Graphene

Powdered graphene was manufactured by researchers from IPFN - Instituto de Plasmas e Fusão Nuclear, project **PEGASUS** - Plasma Enables and Graphene Allowed Synthesis of Unique nanoStructures. [52]

3.2. Methods

3.2.1. Sample preparation

DIN90MnCrV8 steel samples with dimensions of approximately 1.5 cm x 1.5 cm x 2 mm (length x width x thickness) cut from a steel block with a mechanical saw. The first thing done is to acquire a flat surface. We polished the sample with 120-2400 sandpaper, then 6 and 3 µm RAM diamond suspension cloths were used, and finally, we use OPS.

The polishing sample was clean with soap and dried with an air dryer and placed in a beaker with acetone on the ultrasound for 5 minutes.

3.2.2. Surface texturing

We use a femtosecond laser to acquire the surface texturing of the tool steel. The laser used in this experimental activity was a pulsed light Yb: KYW laser (Amplitude Systèmes S-Pulse HP). This laser belongs to the solid-state laser family and is composed of one ytterbium-doped potassium and yttrium tungstate crystal with wavelength 1024 nm and gaussian distribution. The characteristics of this laser and the processing conditions used for surface texturing of the samples are in table 6.[5]

The sample is 15 mm above the focal lens of 150 mm in length. To attain complete coverage of the sample continuous linear scans were made along the Y direction, with each scan having a lateral displacement of the table in the X direction, causing partial overlap of the consecutive tracks. The processing parameters were chosen based on the previous work by Ana Beatriz Ferreira.[5] Samples were textured with LIPSS oriented in the perpendicular orientation to the polarization direction of the laser beam[5].

Table 6 - Laser processing conditions used in steel surface texturing.

Parameters					
Pulse Duration	Average beam power	Sample scanning speed	Laser pulsation frequency	Side table offset, dlat	Processing environment
≈ 560 fs	75 mW	1 mm/s	100 Hz	50 µm	air

3.2.3. Airbrush

A dilution of graphene oxide water dispersion with ethanol 1:1 was prepared and stirred for 20-30 minutes. To deposit the graphene solution, we use a Double action trigger gravity airbrush (KKmoon 100-240V AeróGrafo compressor professional, Pintura artística, Pistola de pulverización modelo), figure 9, and used the following parameters.

Table 7 - Airbrush characteristics.

Distance from sample	Input	Air output	Maximun Pressure	Nozzel diamiter
13-15 mm	100-250V, 50/60Hz, 0,6A Max	10 Lpm	25 psi	0,3 mm

Figure 9 – Airbrush used in deposition methods.

For the graphene oxide samples, we deposited six layers, and we deposited forty layers for graphene samples where each layer dried in air and at room temperature. Figure 10 is a layer deposition scheme where the yellow and orange color corresponds to a 90-degree rotation to create the most homogeneous coating possible.

Figure 10 - Scheme of the layer deposition where yellow and orange represent 90-degree rotation.

3.3. Nanotribometer

The CSM instruments nano tribometer uses a fixed ball in alternating motion sliding in the flat surface under a given load, with perpendicular and parallel direction to the LIPSS. We also attain SEM images of undamaged areas, which allow us to have a better understanding of surface topography after deposition.

In the tribometer, the lever, figure 16, acts as a friction sensor in the horizontal direction, being pressed against the sample surface with a static force exerted by a piezoelectric actuator. During the test, optical displacement sensors measure the deflection of the arm in the vertical and horizontal direction. Since the stiffness of the lever in both directions is known, we can calculate the normal and tangential forces c from the corresponding deflections.

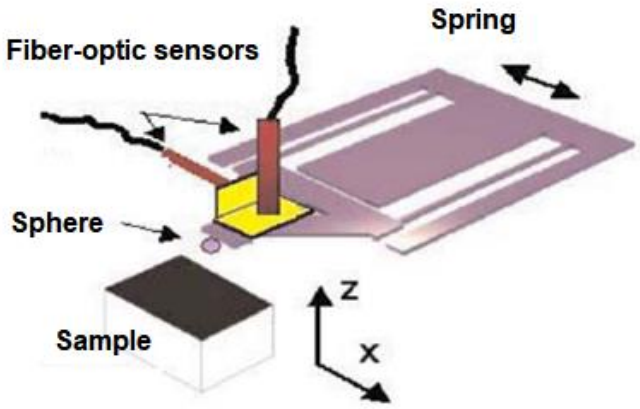

Figure 11 - Schematic illustration of the nano tribometer. Adapted from [63]

During the wear tests, the temperature and relative humidity of the air were measured as these parameters can influence the oxidation state of the surfaces and, consequently, the wear mechanisms. Table 8 shows the recorded temperature and relative humidity values.

Table 8 - Temperature and relative humidity of the nano-wear tests.

Polished Steel	LIPSS + Perpendicular alignment	LIPSS + parallel alignment	LIPSS + Perpendicular alignment + GO	LIPSS + parallel alignment + GO	LIPSS + Perpendicular alignment + Gr	LIPSS + parallel alignment + Gr
Temperture	26.4 ± 0,4	18 ± 0,8	24 ± 0,7	20 ± 0,4	23 ±0,6	21 ±0,2
Humidity (%)	67 ± 5	54 ± 4	50 ± 3	57 ± 6	52 ± 1	54 ± 1

4. Results and discussion

4.1. Wettability tests

Although this work does not focus on the wettability of this type of surface, we need to have some understanding of it. The test were carry out for both polished and textured surfaces using the same steel and the same FS parameter.

Sample A (control) and B (texturized) with water drop with a volume between 0,003- 0,004 cm3 and the contact angle were measured eight times in 30 seconds. Before the tests, all the samples stayed in a vacuum.

The three drops in sample A had no variation of direction since this sample was untreated. In sample B, they use two alignments to see the evolution of the CA with the LIPSS alignment. The Y-direction had three drops analyzed, and the direction X had six drops analyzed to get precise results.

The wettability results show that on a polished surface, the contact angle is 70° degrees and suffers a reduction of 20° degrees after 30 seconds. In texturized surfaces, they observed a contact angle higher than 135° degrees and an average decrease of 3° and 4° degrees on the first 30 seconds for on Y and X alignment, respectively.

These results will allow us to better understand the different wettability mechanisms presented in polished and LIPSS samples.

As explained earlier, an application for LIPSS is to control the wettability of a given material. A wettability test was done on my LIPSS, allowing us to see that the texturized surface becomes hydrophobic, showing contact angles higher than 90 degrees. The difference of coating can be explained by the hydrophobic effect combined with the energy/momentum that a atomize drop of Gr solution has after ejection from the nozzle.

A stream of compressed air passes through the airbrush; the Venturi effect creates a local reduction in air pressure that allows liquid to be sucked from the dispersion cup. The high velocity of air atomizes the solvent comprised of graphene into very tiny droplets as it blows past the nozzle.

On a polished surface, the ejected Gr sheets are transferred from the atomized droplets onto the surface after we allow the solvent to evaporate and dry. We restart the process atomized ejected droplets of Gr dispersion from the nozzle will come in contact with Gr sheets that are deposited and bonded with weak (Van der Waals) forces to the surface.

The droplet energy/momentum is enough to break that bond or Van Der Waals forces between Gr and surface, and yanks, push, or drags the Gr sheet that is deposited on the surface from the initial position to a secondary position.

The Gr sheets that can overlap, stacked, or agglomerate inside the liquid medium after drying will transfer the Gr to the surface. The hydrophobic natures of the metal surface and the deposition angle of the airbrush will have a tremendous effect on this phenomenon.

On a textured surface, this mechanism/theory acts a little bit differently between LIPSS and the graphene sheet. The atomized Gr droplets enter in contact with the grooves pushing the air trapped between channels out. The droplet energy/momentum transferred to the Gr sheet and the collision between Gr sheets and the textured surface generates higher adhesion forces than before, minimizing or preventing this way the change in position. I can even contemplate that some graphene sheets can act as a claw/grip on the grooves or even lodged themselves in the groove's channels.

After an x number of deposition cycles (x number of layers), there will be a uniform/continuous coating. The (x+1) deposition cycle will interact with the graphene coating instead of the grooves. The adhesion mechanism between graphene sheets and coating depends on the roughness that is attained after x number of layers.

4.2. Coating methods

In this chapter we evaluate two coating deposition techniques for graphene-based lubricants and demonstrate the failures and problems that have arisen. There are many studies about deposition methods such as chemical vapor deposition (CVD), electrophoretic deposition (EPD), solution spray, dip coating, spin coating, drop-casting. Nevertheless, the procedures that we chose and applied will be the most suitable to deposit GO or Gr on a metal substrate to act as a solid lubricant.[48][49]

Drop Casting: Drop cast deposition consists of using a syringe to drop droplets of a liquid solution on a metal surface.

This method is promising in film deposition for tribology wear and friction. A combination of flexibility, and substrates deposition with different sizes and shapes convert this into one of the two simplest

methods to manufacture Gr based coatings. The flaws presented in this technique are the adhesion between the substrate and coating, or the forces present are weak and lead to the fast removal of the coating during the process. [48][53][54]

This method was not suitable for our needs because the coating was dried in air or in a desiccator for 24 hours, generating a uniform film with flaws/defects, figure 11 (A). We see four problems: (I) the boundaries of the film shows surface oxidation, probably due to chemical interaction between graphene oxide solution in water and the steel; (II) after drying, we observe uncoated areas; (III) small openings/absence of lubricant; (IV) figure 11 (B) show numerous cracks in the GO coating, created during the drying process. During the drying process, the surface tension imposes stress, which exceeded the max stress that the thin GO film can bear. One other cause can be the poor adhesion between the GO film and surface producing internal stress that creates delamination's.

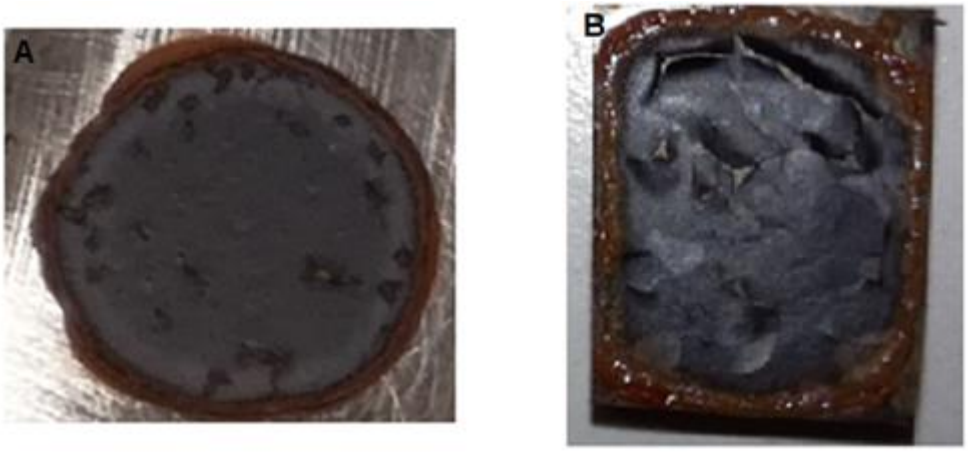

Figure 12 - GO film created by drop-casting method. (A) solid GO film and (B) Delamination of GO film.

After, we use this method and graphene, figure 12, we see that the wettability properties of the surface favor the agglomeration between Gr sheets, making this method ineligible for our work.

Figure 13 - Graphene agglomeration attains after the drop-casting method on a polished surface.

Spray coating: This simple deposition technique uses a spray gun, like an airbrush to create a coating on the surface. In comparison with the drop cast, this method provided a more homogeneous coating and giving us better control over the film thickness.

Rheological properties of the dispersion like density, surface tension, and viscosity can influence the process quality of the coating. It can also be affected by process parameters, such as the spray pressure and distance to the sample, spray time and temperature, as well as the characteristics of the substrate, wettability, etc.

After the dried process, it is possible to see, in figure 14, some brighter and darker areas. The dark regions correspond to the GO deposition and agglomeration while the brighter zones correlate to the light reflected by the camera flash in the polished metal surface. This means that on those regions, the GO coating was thinner or nonexistent.

Figure 14 - GO coating defect exhibited on the polished surface created by spray deposition.

Figure 15 displays the surface coating obtained after Gr spray deposition on the textured surface with different layers.(a) (b) an (c) are 5, 20, and 40 layers, respectively.

Figure 15– Surface characteristics for LIPSS coated with graphene. (a) 5 layers; (b) 20 layer; (c) 40 layer.

.

In figure 16, it is possible to see the difference, after 40 layers, between (a) polished surface and (b) textured surfaces with LIPSS. One of the most noticeable things is the lack of graphene in the center of the sample shown in figure 15 (a), explained in chapter 4.1, even after 40 layers, while in figure 15 (b) Gr coating covers the entire surface of the LIPSS.

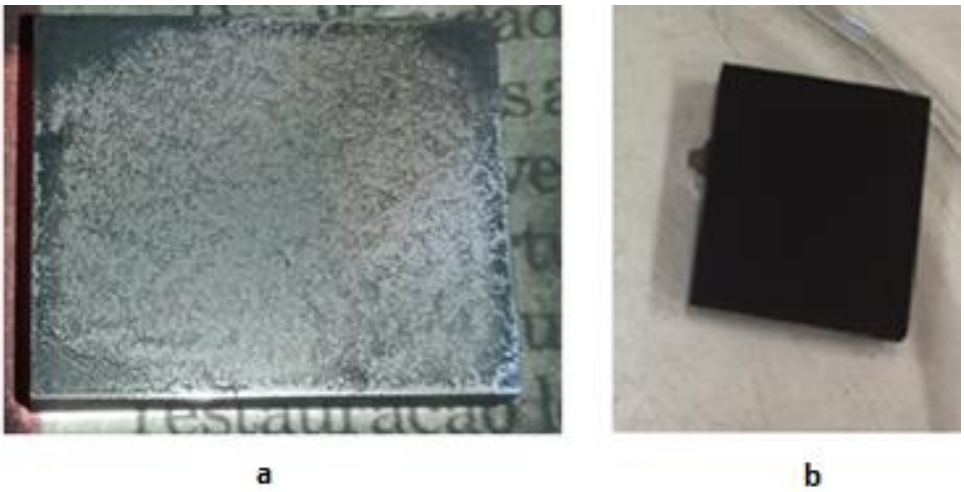

Figure 16 – Surfaces coated with Graphene. (a) polished; (b) LIPSS textured surface.

4.3. Polished surfaces

Figure 17 shows the evolution of the friction coefficient for polished surfaces during 2000 cycles with 10 and 25 mN loads.

The COF evolution clearly shows that 25 mN has a lower COF and an analogous behavior to the run with a load of 10 mN. The run-in period consists of a sharp increase in friction coefficient in the first cycles from 0.5 to 1.1, followed by an almost stationary regime near cycle number 150.

Between 150 and 400 cycles, there is an increase in the friction leading to the highest friction coefficient attained, and between 400 and 600 cycles the friction coefficient drops to a lower value.

Throughout the test, there is an almost sporadic increase and decrease in friction coefficient together with a stick-slip phenomenon. For 25 mN load, we have an increase in COF from 0.3 to 1 preceded by a reduction to a lower plateau around 180 cycles. We have a 0.8 COF steady-state regime until the end of the test with the presence of a stick and slip phenomenon.

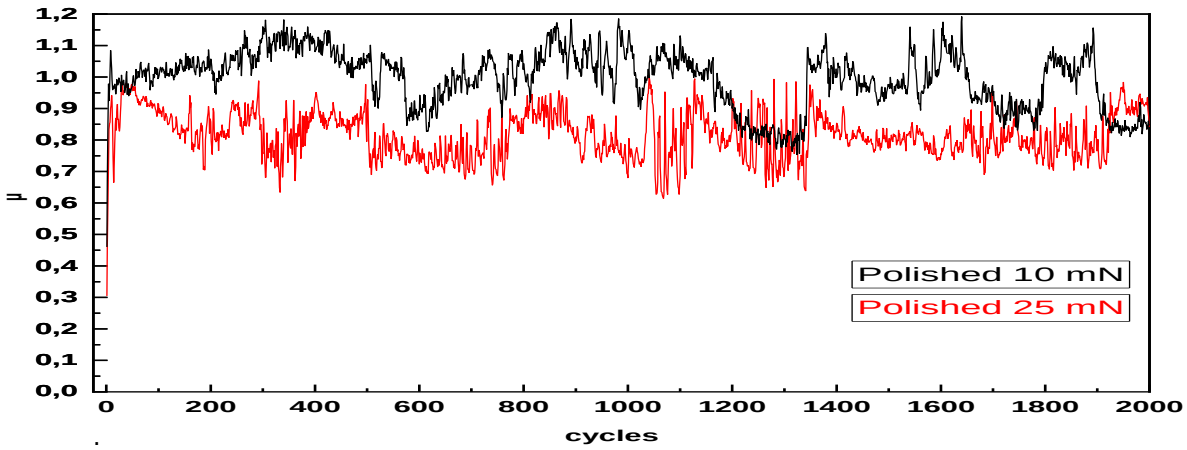

Figure 17 – Friction coefficient evolution for polished surface during 2000 cycles and with 10mN and 25 mN load.

This increase and decrease in friction behavior shown in figure 17 are the same as seen in chapter 2.2.1.1, curve type (III), that associates the increase in friction with the generation and entrapment of wear particles followed by a drop in friction that corresponds to the ejection of those wear particles. The process repeats itself over and over during the test.

If we look at the evolution of COF with a load of 25 mN the friction coefficient appears to be almost stationary, only breaking this behavior when presented with a stick and slip phenomenon. We have a faster generation/entrapment of wear particles followed by their ejection, this occurrence is less obvious, and it takes fewer cycles to accomplish.

The tribometer displays the friction coefficient as a function of time. During this process occurs a phenomenon called stick-slip motion. Adhesion between surfaces generates a surge in friction force, thus promoting a sharp increase in friction coefficient.

When the applied tangential force by the mechanism turning the specimen is enough to overcome the adhesive bonds at the interface, fracture occurs, friction force starts do drop, and the slip associated with the stick-slip motion arises very rapidly.[12][13][14][43]

The cohesive strength and surface energy of the sliding determine the stick-slip amplitude, and the process repeats itself over and over during the test.

Figure 18 depicts an image of a polished surface described in chapter 3.2.1. In the figure, it is possible to see one tiny hole one has the shape of a diamond.

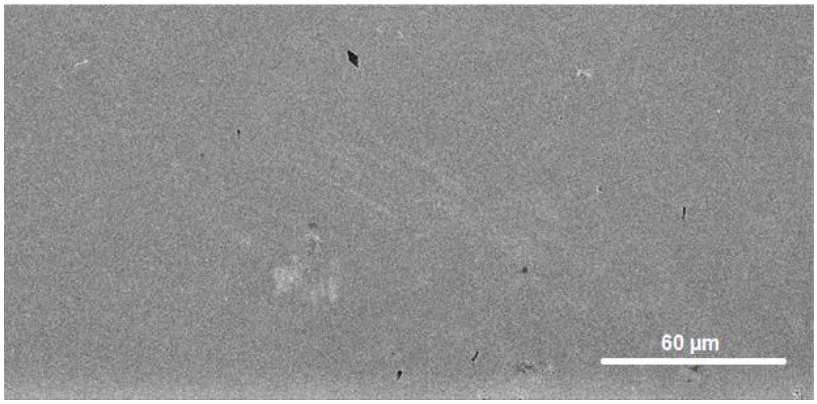

Figure 18 - SEM images of the polished surface.

Figure 19 (A) shows a track that can be divided into three different zones. The first corresponds to the center, where the radial distribution of the contact pressure in the sphere-to-plane contact is maximum and gradually decreases from the center to the periphery. As the contact pressure increases in the center of the track, the temperature at the interface will increase, creating an environment that promotes oxide particles. The second relates to the little or undamaged section that is caused by low contact pressure between the surface and the periphery of the sphere.

The third correspond to the ejected wear particles that form the outer part of the track. In figures 19 (A) and 20 (A), we can see the ejection of wear particles limiting the top and bottom part of the track, and we see an accumulation/gathering on the edge. Which is explained by sphere-to-plane configuration with a movable table that pushed the particles to the margins. Figure 19 (A) and (B) and figure 20 (A) and (C) both confirm the presence of small bright spots, wear particles that can be found in the middle of the track.

Adhesive wear is foreseeable since stick and slip behavior is present in figure 18. This type of wear can be seen in figure 19 (A), which shows oxide particles coupled with adhesion wear.

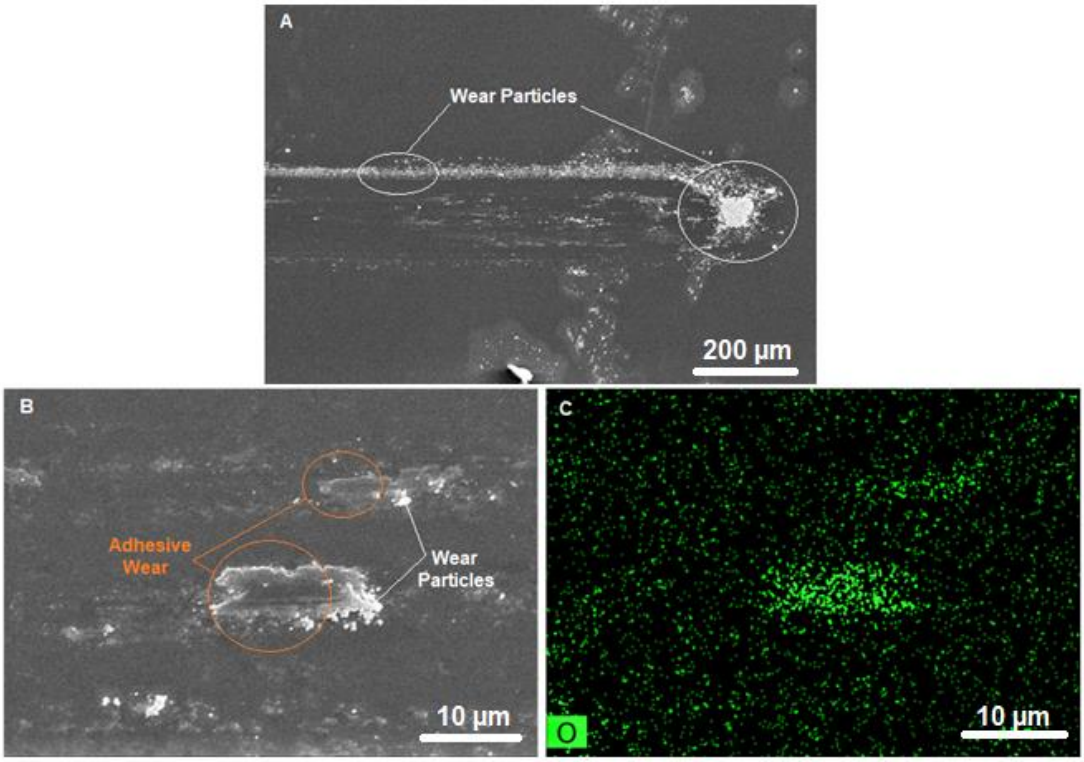

Figure 19 -Wear track obtained after 2000 cycles with 10 mN load of the polished surface. Image (A) and (B) are SEM images (C) is the EDS oxygen map.

Figure 20 (B) shows minor adhesive wear coupled with wear/oxide particles. Figure 20 (A) and (B) displays the 25 mN track limited by oxide particles comparing both figures (A), we observe that the 25mN load test has a higher concentration of wear particles at the extremities. I attributed the increase in particle volume to the increase in load that can destroy the tribo-film faster, promoting this way an increase in wear particles, temperature and friction.

In this test, we have two different types of wear. If we look at figure 20 (A) and (C) it is possible to identify the abrasive wear, 2 or 3 longitudinal grooves in the center of the track, most likely due to micro- plowing. The abrasive wear attained is attributed to the load combined with the production and entrapment of particles between the sphere and matrix.

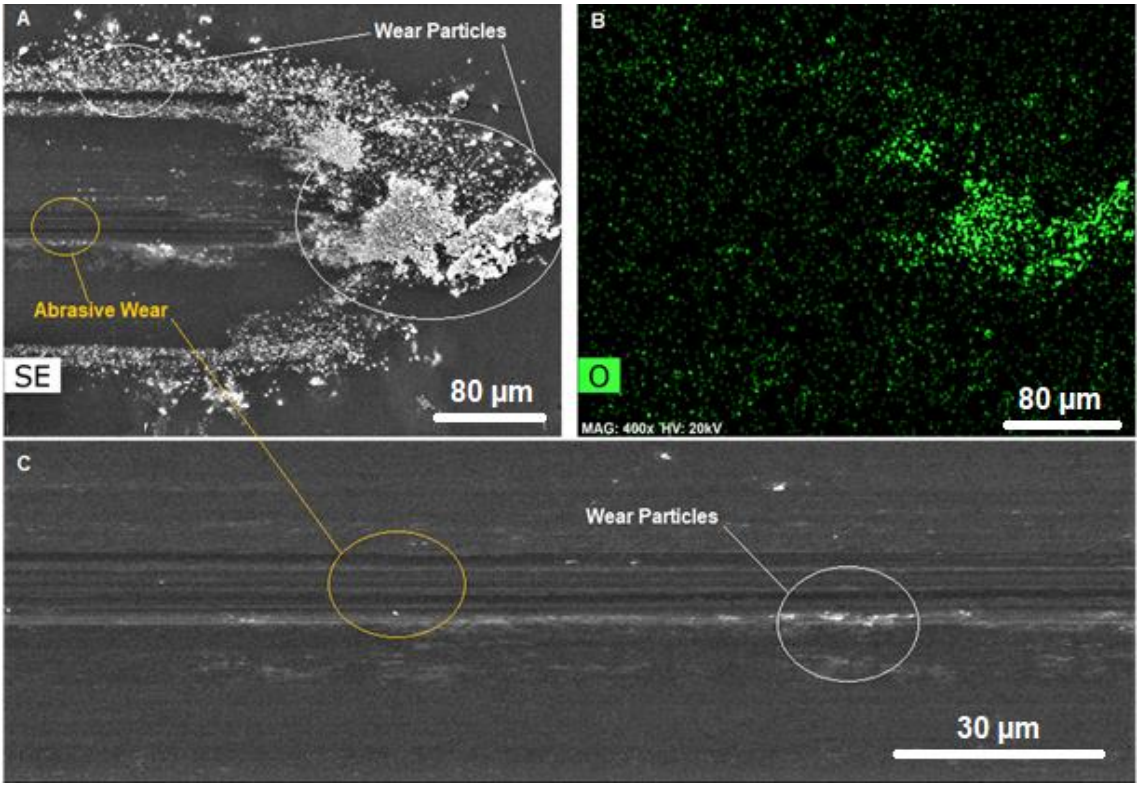

Figure 20 - Wear track obtained after 2000 cycles with 25 mN load of the polished surface. (A) and (C) are SEM images (B) EDS oxygen maps.

4.4. Polished surface coated with graphene oxide

Figure 21 displays the friction coefficient evolution for polished surfaces coated with GO with 10 and 25 mN load. The 10 mN load COF graph shows strange oscillations in the first 60 cycles that correspond to sharp increases and decreases in friction, between 0.5 and 0.8.

Looking at the COF evolution with 25 mN load we see the opposite behavior, a sharp decrease in friction coefficient, from 0.8 to 0.5. Both behaviors can be associated with the early cycle interaction between sphere and coating. Liang, Hongyu [55] demonstrates that the COF attained seems to be correlated to the roughness of the film, where the rougher film is the higher the coefficient. After this, both loads presented similar COF values, where there is a steady state regime with a COF value between 0.4 and 0.5, that embody friction on GO film.

After this regime, the GO film is damaged, destroyed, or pushed to the sides. Metal surfaces enter in contact with one another and we attain the first transition period. Finally, we achieve the second steady state regime that has a friction coefficient between [0.7;0.9] and [0.65;0.8] for 10 mN and 25 mN respectively. Once again, the increase in load produced a lower coefficient of friction (COF).

Further analysis shows that the increase in load promotes the destruction of the GO layer in the earlier cycles. We observe stable COF oscillations attributed to the presence of lubricant coating and after the initially protective period, the sliding contact areas began to experience more and more steel to steel contact, resulting in a more unstable/stick and slip phenomenon.

Similar to our work Berman, Diana[56][57] and Zheng, Dan[58] observed a reduction in friction coefficient with reasonably stable frictional behavior by adding graphene-based lubricants to the interface.

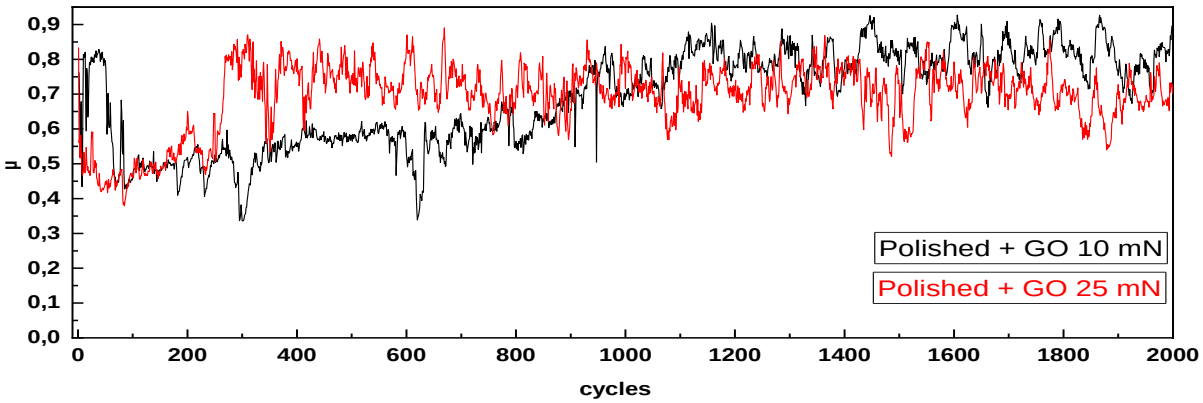

Figure 21 - Friction coefficient evolution during 2000 cycles with 10 and 25 mN loads of the polished surface coated with graphene oxide.

Figure 22 displays the SEM images with EDS oxygen and carbon maps for a polished surface coated with GO. Looking at figure 22, we see a surface covered with GO contains some wrinkles, a phenomenon commonly observed in coatings done by spray deposition.

There are two types of mechanisms to form Wrinkles. (I) Staking where graphene film is not homogeneous and promotes a progressively growing wrinkle in the film, or (II) folding where the graphene sheet folds on itself, creating a small wrinkle that will grow with the increase of layers.[51][59]

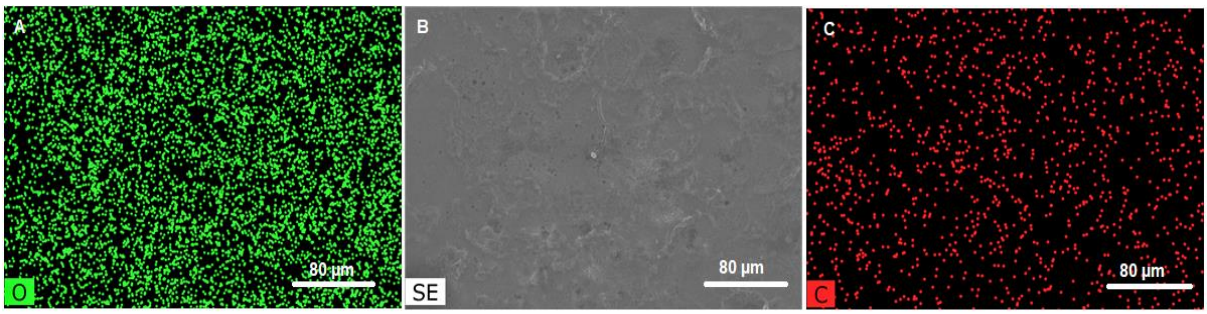

Figure 22 - SEM images of the polished surface coated with graphene oxide. (A), (C) EDS oxygen and carbon maps, (B) SEM image.

The major problem that wrinkles cause is the same that we see in the puckering effect. The increase in the contact area, due to wrinkles formation, leads to graphene sheets being partially pulled, due to Inter-atomic forces along with the tip.

Similar to Diana Berman[57], figure 23 (A) illustrates the wear track attained for 10 mN and shows that the alternating movement of the sphere over the sample pushes a higher concentration of GO coating to the extremity of the track. Figure 23 (B) and (C) exhibit the EDS oxygen maps, where we observe the absence of GO in the center of our track, the reason that the carbon map his less pronounce is because it difficult to extract a good EDS carbon map using the SEM machine.

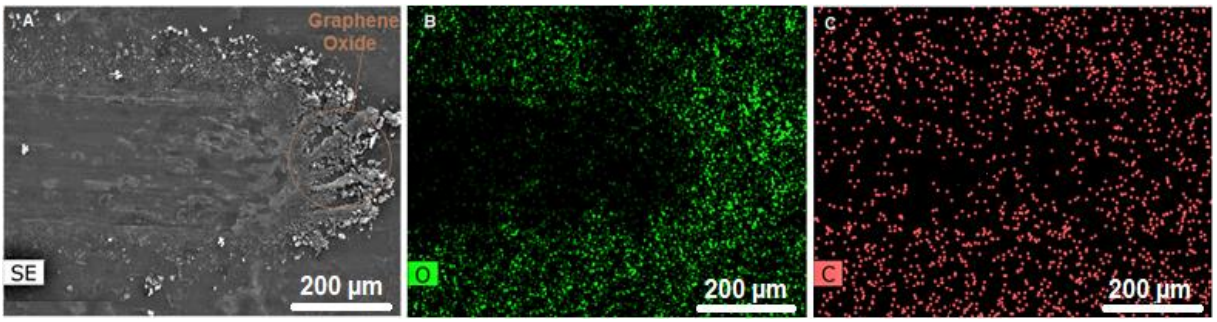

Figure 23- Wear track obtained after 2000 cycles with 10 mN load on the polished surface coated with graphene oxide. Images (B) and (C) are EDS carbon and oxygen maps.

Figure 24 allows us to observe three different areas that are present after the 2000 cycles. (I) on the left side, two small areas with, what seems to be, small grains on the surfaces, which corresponds to GO combined with oxide particles; (II) on the right side, we have some areas that are flat without foreign elements that correspond to the tribo-layer. Finally, (III) small regions with a crack that is GO film with little or no damage.

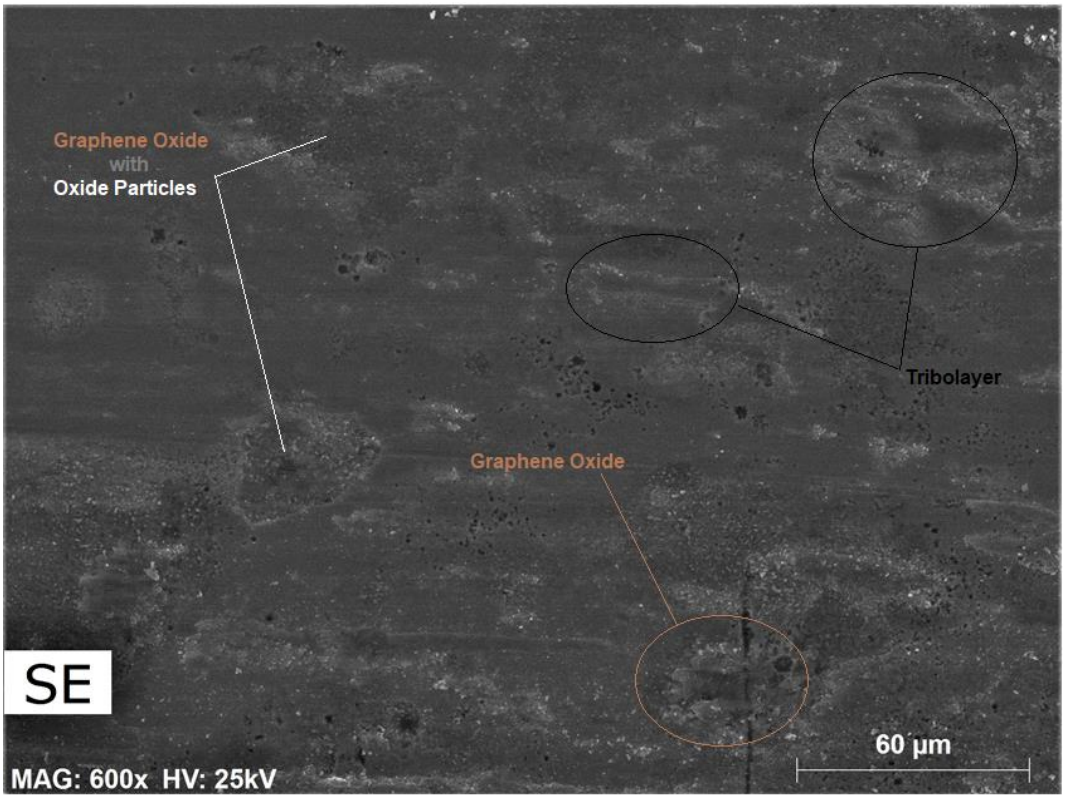

Figure 24 - Wear track obtained after 2000 cycles with 10 mN load of the polished surface coated with graphene oxide.

Analyzing figure 25 (A), 25 mN load backscatters image, we see some small almost spherical zones that I believe to be graphene oxide spots. Figure 25 (B) oxygen map that shows a smaller oxide layer in the center of the track that supports the claim that occurred contact between surfaces and existence of stick and slip behavior in figure 21.

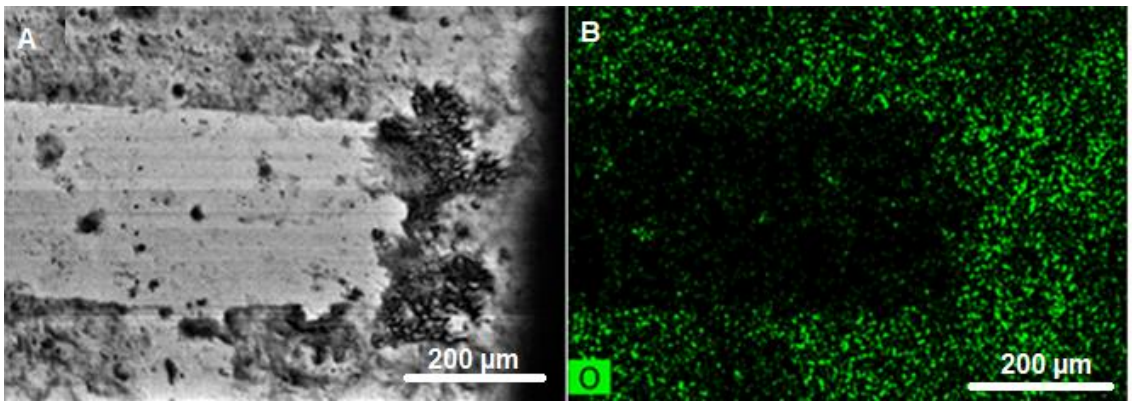

Figure 25 - Wear track obtained after 2000 cycles of the polished surface coated with GO and 25 mN load. (A) BSE image and (B) Oxygen map images

Figure 26 depicts the wear track and helps support the claim that the track is limited by undamaged GO coating. Shows two areas that resemble adhesive wear created by the alternating movement of the sphere over the sample. Taking a closer look at the center of the track, we see that there are small zones with GO that are still present after 2000 cycles.

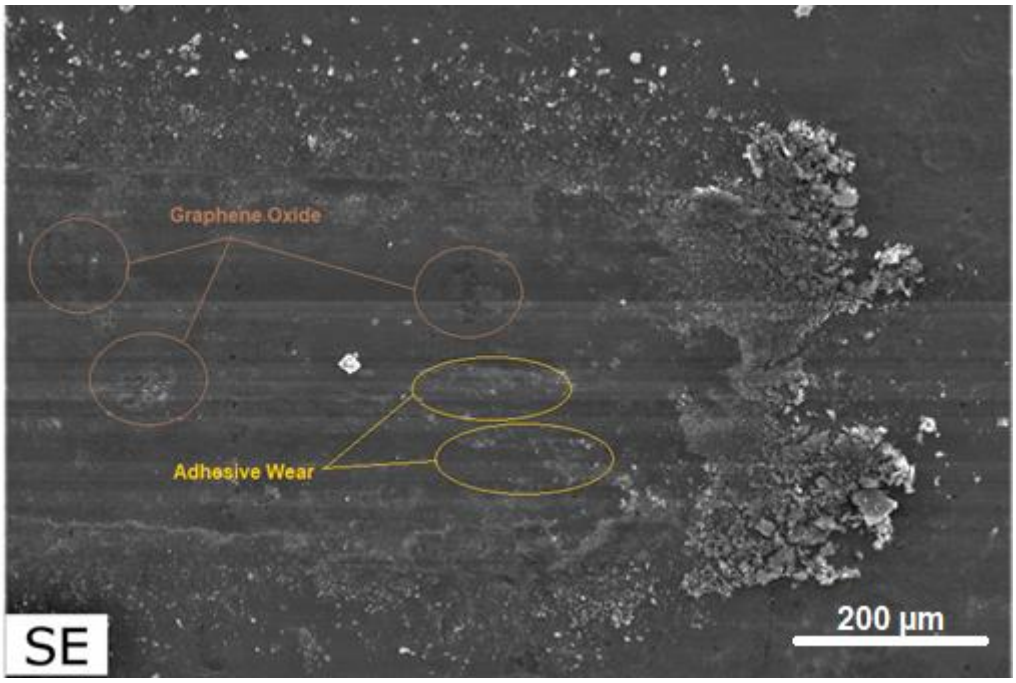

Figure 26 - Wear track obtained after 2000 cycles of the polished surface coated with GO and 25 mN load.

4.5. Polished surface coated with graphene

Figure 27 represents the friction coefficient evolution during 5000 cycles with 10 and 25 on a polished surface coated with graphene. The COF attained in for 25 mN load was lower than the 10 mN load, and since the typical S-shaped curve was not achieved I assume that metal to metal interaction did not occur.

The run-in period corresponds to a drop in friction coefficient from 0.75 to 0.4 in both cases. In the 10 mN load, we have a steady state regime with a friction coefficient between 0.4 and 0.55 going until the end of the test. However, looking at the friction curve for 25 mN load, we see an increase in friction in the first 500 cycles followed by sharp decrease in friction and a steady state regime until the end of the 5000 cycles.

The sharp decrease in COF is explained by the creation of a thick and solid Gr layer and instead we have an interaction between two Gr layer we have interaction between solid gr layer and the sphere, the decrease in COF is related to the destruction of this layer and subsequent change in friction system.

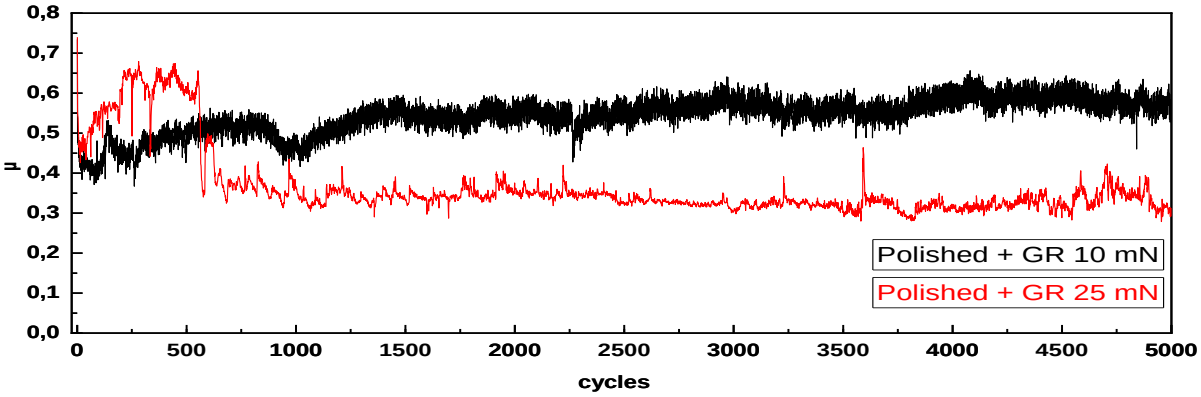

Figure 27 – Friction coefficient evolution during 5000 cycles with 10 and 25 mN loads on the polished surface coated with graphene.

Figure 28 shows the SEM images and the carbon map for polished surfaces coated with graphene. We immediately observe that the Gr coating did not cover the totality of the sample. We attributed this lack of graphene to (I) that graphene dispersion in alcohol solution was not the best or (II) this method leads to a Gr cluster in the surface.

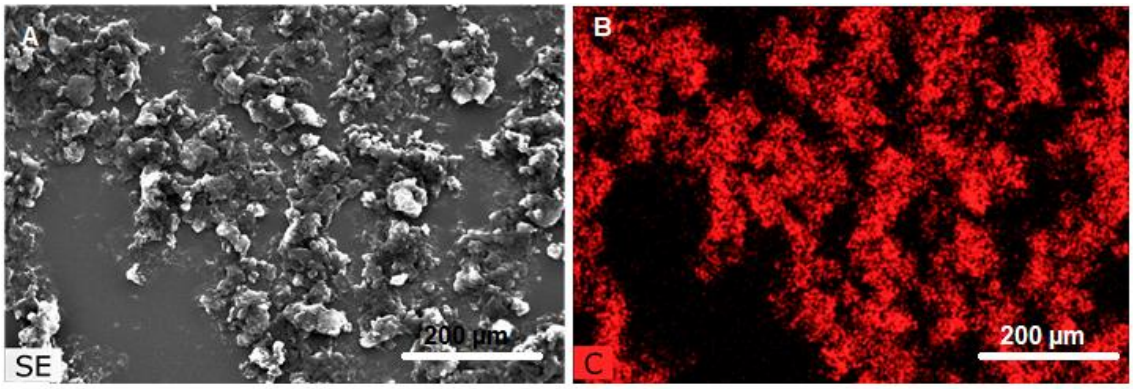

Figure 28 - SEM images of the polished surface coated with graphene. (A) SEM image, (B) EDS carbon map.

If we look at figure 29 (A), we observed that the pushed Gr coating acts as boundaries of the track. There are two effects need further explaining: (I) the darker areas in the left part of the track are Gr accumulations; (II) on the right side of the track figure 29 (B) and (C) appears to be a small tribo-film above of a small area of GR. The tribo-film is attributed to the metal to metal interaction created by the lack of graphene in that region.

For every accomplished cycle, small GR sheets detach from the coating layer which ensures that there is no contact between surfaces and guarantees the same friction behavior. This performance paired with the friction coefficient evolution leads me to assume that the left part of the track had more or a thicker Gr layer then the right side. When the sphere reaches the right side of the track with little or no GR attached to it, there is metal to metal contact that creates the tiny tribo-film exhibited. This

phenomenon repeats itself over and over with the same stick and slip behavior throughout the test. Similar effects can be seen in [25][57][60].

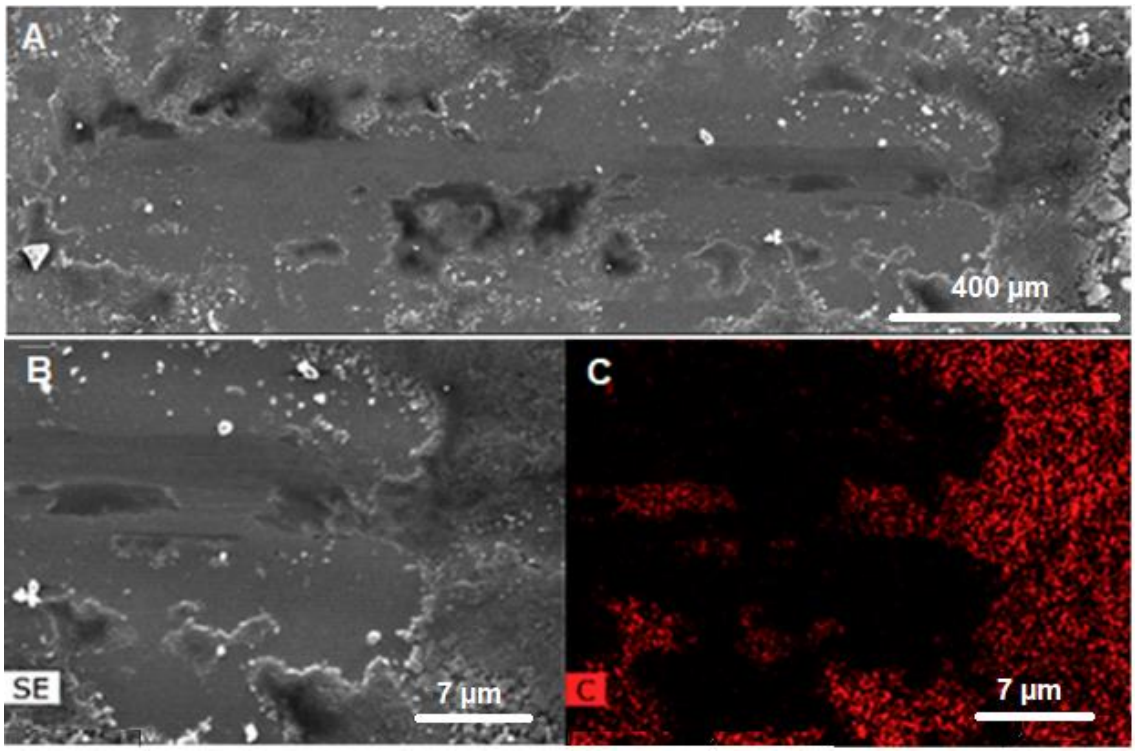

Figure 29 –Wear track obtained after 5000 cycles with 10 mN load of the polished surface coated with graphene. (A) and (B) SEM images, (C) carbon map.

The figure corresponding to the 25 mN friction curve shows the same behavior, but without the film tribe and as the so-called solid layer was destroyed in previous cycles the figure shows nothing new and will not be shown. However, to better understand what type of conduct occurs when there is a greater or total lack of RG on the surface.

As explained earlier, it is necessary to consider the zone where the test takes place so that we can study the wear marks of tests with fewer cycles performed in areas with less Gr.

Looking at the evolution of the friction coefficient, figure 30 shows the evolution of the COF with loads of 10 and 25 mN, where we can see a stable COF throughout the execution of the test for the load test of 10 mN. Where there is the first steady state regime with a friction coefficient of 0.5 and after 1400 cycles, there is a transition period, the interaction between metal surfaces, leading to a second steady state regime with a COF between [0.7; 0.8].

While in the 25 mN load, we have a lower but strange steady state regime until 400 cycles. After a stip transition period between [0.6; 0.9], we have an unstable and almost periodic COF. Although the different number of cycles in both loads, we can still see that the COF behavior of each test does not

show any similarities. I attributed these differences to a thinner or previously explained lack of lubricant layer on the test spot that leads to interaction between surfaces.

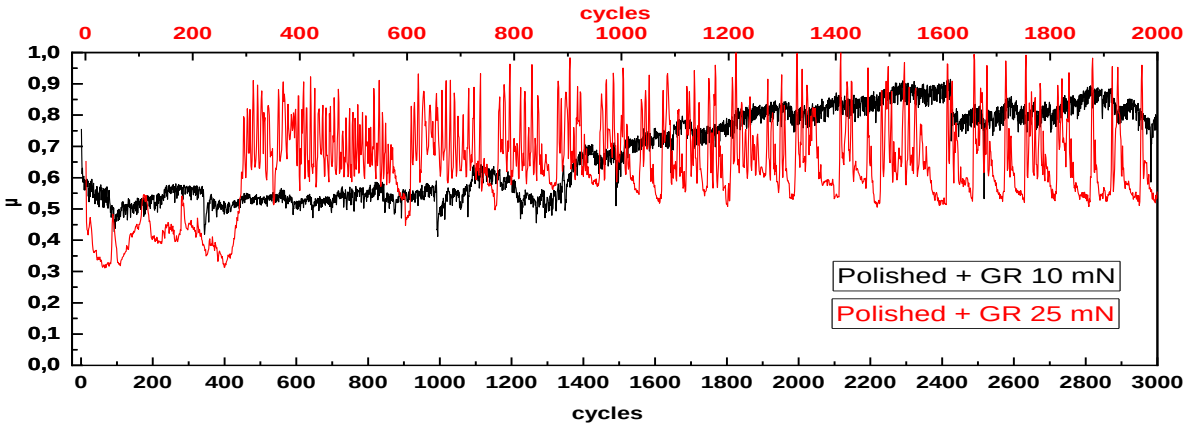

Figure 30 – Friction coefficient evolution during 2000 and 3000 cycles with 10 and 25 mN loads of the polished surface coated with graphene, respectively.

The 3000 cycles wear track, figure 31 (A), can be divided by zones where in the center there is a light grey area that is where the contact was maximum and is restricted by tribo-film. After, there is a clear zone without Gr, most likely caused by lower contact pressure at the periphery of the sphere that easily removes the graphene from the surface pushing it to the sides.

If we look at figure 31 (B, C, D), it is possible to see a magnification of the right side of the track, where the oxygen shows a small oxide zone on the right extremity of the track. In the carbon map, we see a large amount of graphene pushed to the right margins.

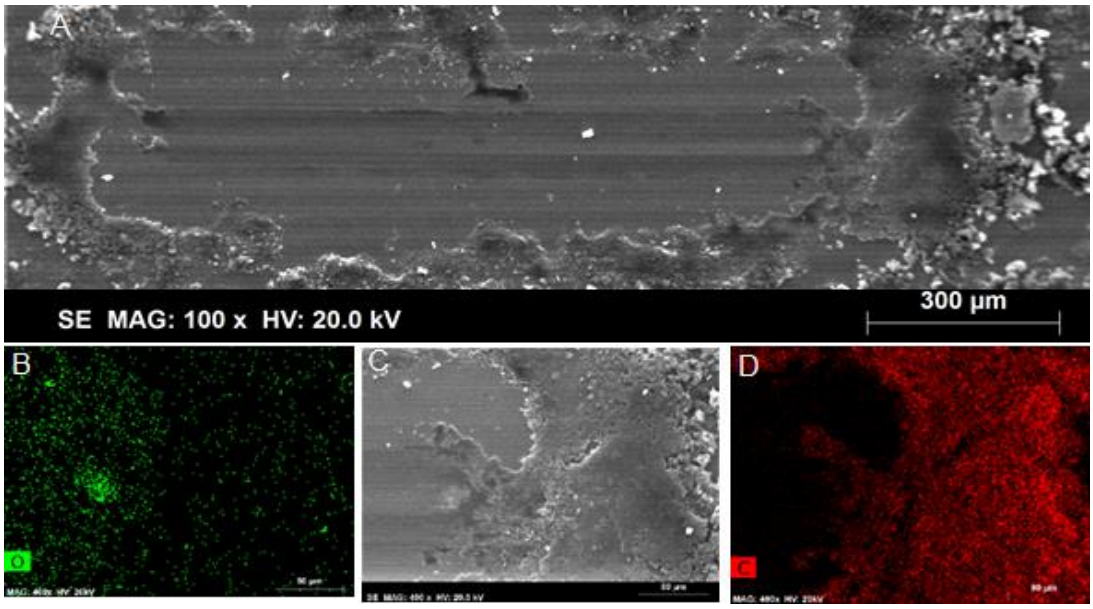

Figure 31 - Wear track obtained after 3000 cycles with 10 mN load of the polished surface coated with graphene. (B) and (D) are oxygen and carbon map.

Figure 32 (A), (B), and (C) displays a small Gr area that enters in contact with the periphery of the sphere after x cycles of wear. We can conclude that Gr film enters in contact with the sphere surface and starts to peel layer by layer until the interaction is lost. This phenomenon can be explained by Liu, Lincong [61], that connects the friction coefficient to the weak van der Waals forces combined with low shear resistance between the adjacent atomic layers allowing it to exhibit ultra-low frictional characteristics.

We also observe what appears to be a continuous oxide film that covers the track. Figure 29 (A), 31 (A), and 32 (A) show similar tribo-films, which corresponds to metal to metal interaction.

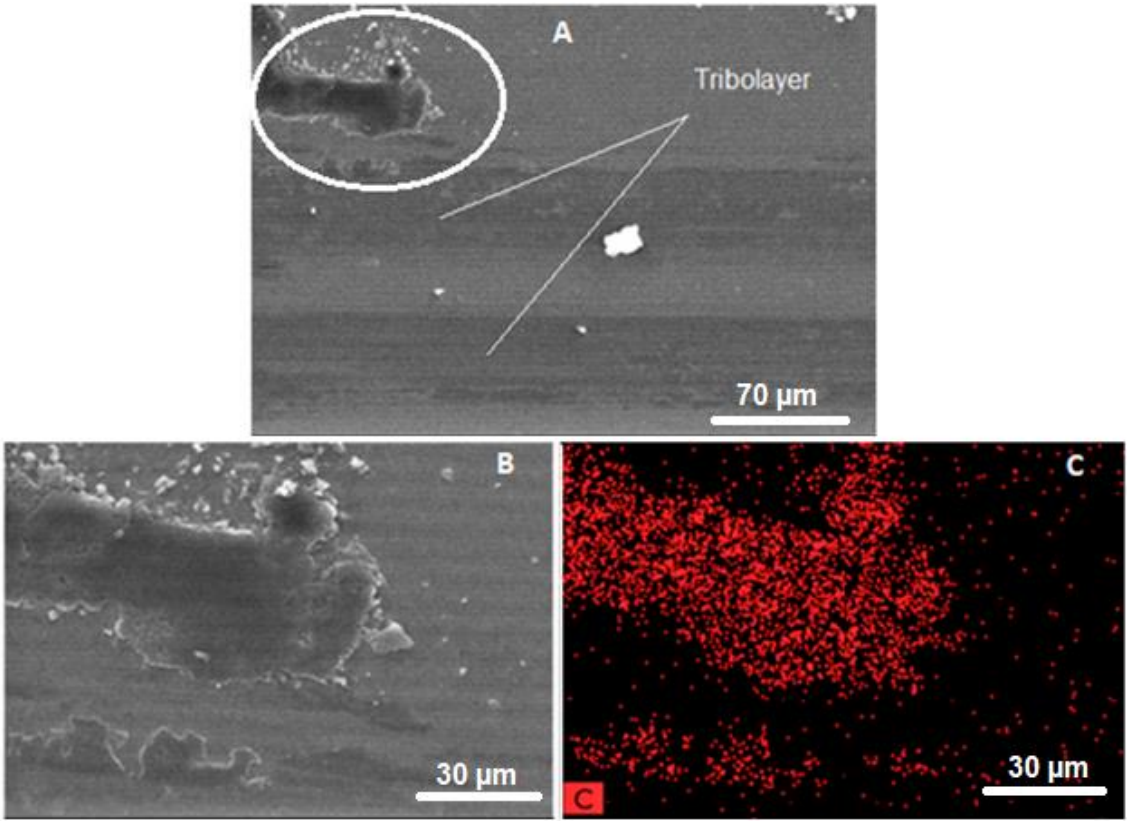

Figure 32 - Wear track obtained after 3000 cycles with 10 mN load of the polished surface coated with graphene. (B) and (D) are oxygen and carbon map.

Figure 33 displays the wear track for polished surface coated with GR with 25 mN load after 2000 cycles. Similar to the one attained in 10 mN. In the center, it is possible to see small zones containing wear particles coupled with what looks like adhesion. On the right side, there is a massive oxide area with two darker spots.

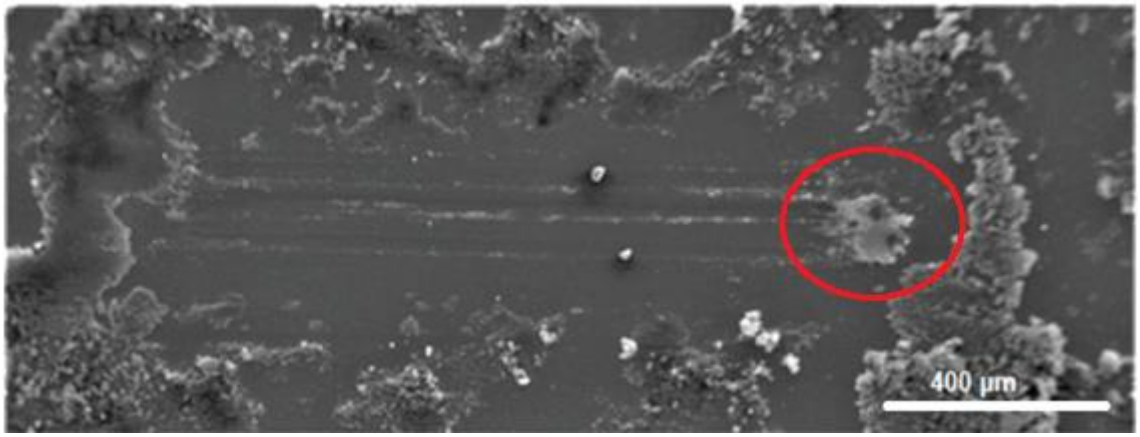

Figure 33 - Wear track obtained after 2000 cycles with 25 mN load of the polished surface coated with Gr.

If we look at figure 34 (A) we have a small adhesive wear zone. We assume that the middle of the track contains traces of adhesive wear surrounded by wear particles similar to this one. We also observe that on the right side of the path, there is one big oxide film that has two Gr spots. These lubricant spots and oxide film contributed to the behavior exhibited in figure 30. Figure 34 (B) and (C) support the existence of graphene on the massive oxide layer.

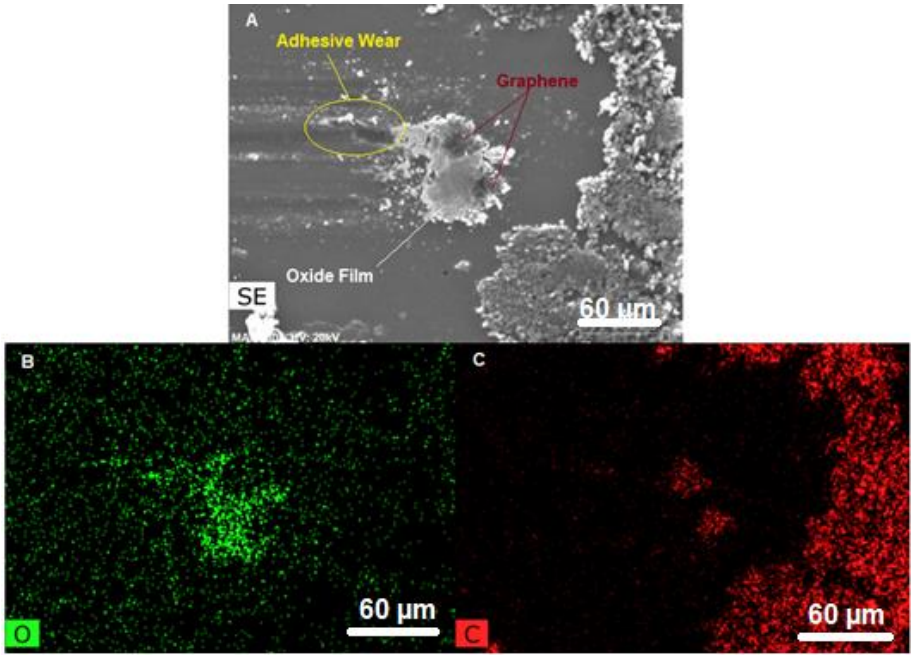

Figure 34 - Wear track obtained after 2000 cycles with 25 mN load of the polished surface coated with Gr. (A) SEM, (B) and (C) oxygen and carbon maps.

4.6. Laser-induced periodic surfaces structures

4.6.1. Parallel alignment

Figure 35 shows the evolution of COF for 10 and 25 mN loads with parallel alignment. We observe that they have similar behavior except in the first 250 cycles.

The evolution for the 10 mN load, we have the first steady state regime until 50 cycles and a friction coefficient value around 0.6. Next, there is a transition period from 50 to 150 cycles until a COF of 1 is achieved. This was the max value attained in this run. From 150 cycles to 700 cycles it is possible to see a reduction followed by an increase and another reduction in friction until the second steady state regime with 0.8 μ is achieved.

For 25 mN load, we observe that the run-in period is a reduction in friction coefficient from 0.5 to 0.4 followed by the first steady state regime until 50 cycles. Next, there is a transition period from 50 to 500 cycles until reaching a friction coefficient of 1. After this, there is a reduction in the friction coefficient achieving the second plateau with a COF between 0.7 and 0.8.

In the parallel configuration, the first steady state and transition regimes are most likely associated with the destruction of the oxide layer, promoting this way contact between surfaces. The decreases and increases of COF values are associated with the plastic deformation of asperities and the production of wear particles due to fracture.

The small increase in friction coefficient after 1600 cycles could be associated with the destruction of tribo layer or with the increase in plastic deformation of LIPSS. This increase in contact area can be explained by Zhuo Wang[33].

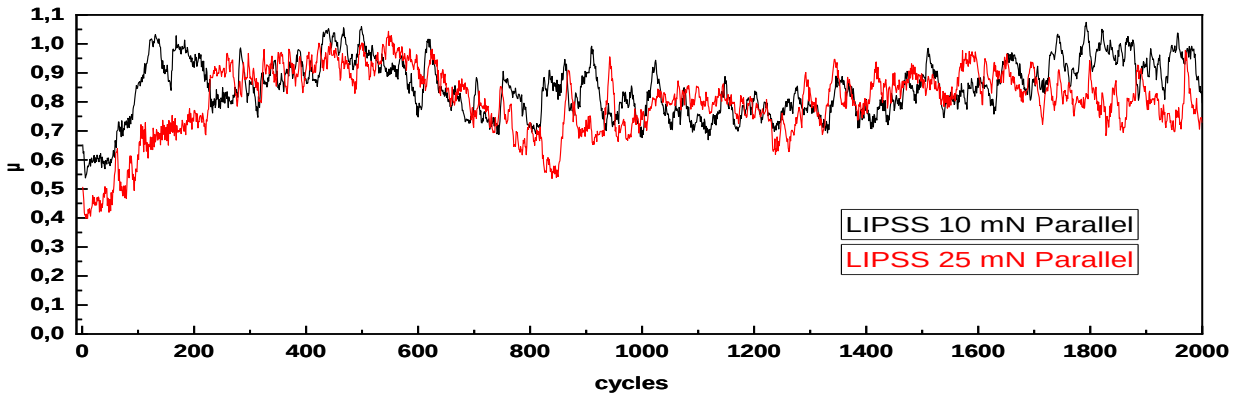

Figure 35 - Friction coefficient evolution during 2000 cycles with 25 mN loads of the LIPSS with parallel alignment.

Figure 36 shows a 3D image for the LIPSS surface attained after using 3D roughness analysis software. We measure and obtain an average period of 1,4 µm between grooves, MPD - Mean Profile Depth of 0,202 µm, and a Ra =0,223 µm

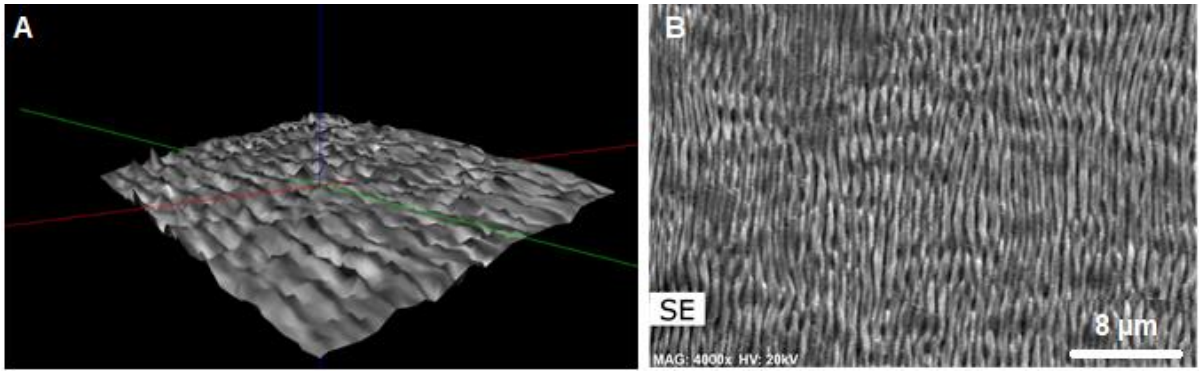

Figure 36 – (A) 3D illustration of the texturing of steel with the femtosecond laser. (B) SEM images of attained LIPSS using the process parameter above.

if we look at figure 37 (A), parallel alignment, we see the tack that is defined by two darker lines. Figure 37 (B) and (C), SEM, and EDS oxygen map, show that LIPSS appears to have small oxide-film spots that avoid any excessive plastic deformation.

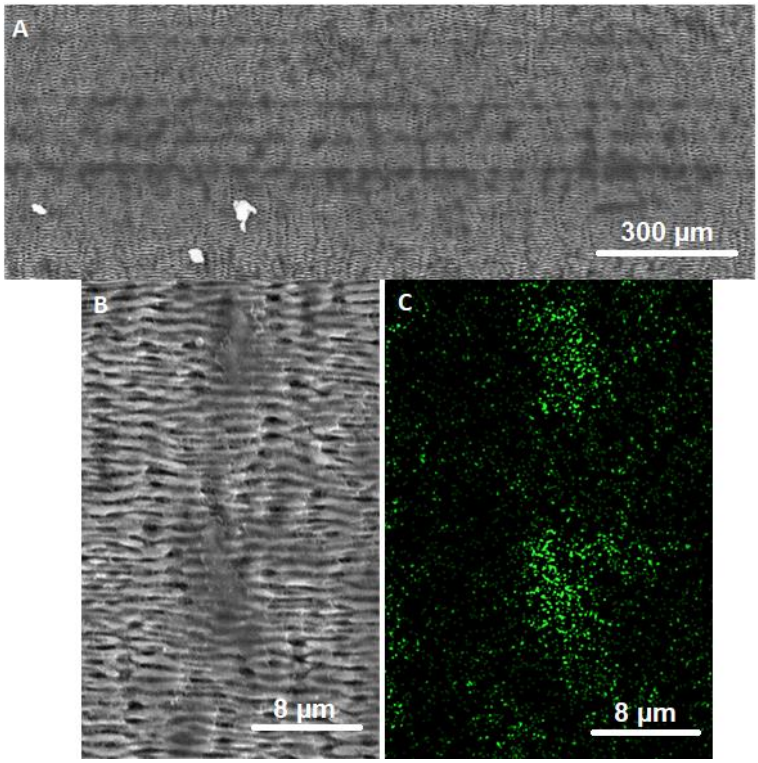

Figure 37 - Wear track obtained after 2000 cycles with 10 mN load of the textured surface with LIPSS, parallel alignment. (A), (B) SEM images (C) Oxygen map.

Looking at figure 38 that displays the wear track for 25 mN load, we observe a similar wear track to the one showed in figure 38 (A). The track appears to have a higher quantity of oxide layer, especially on the left side.

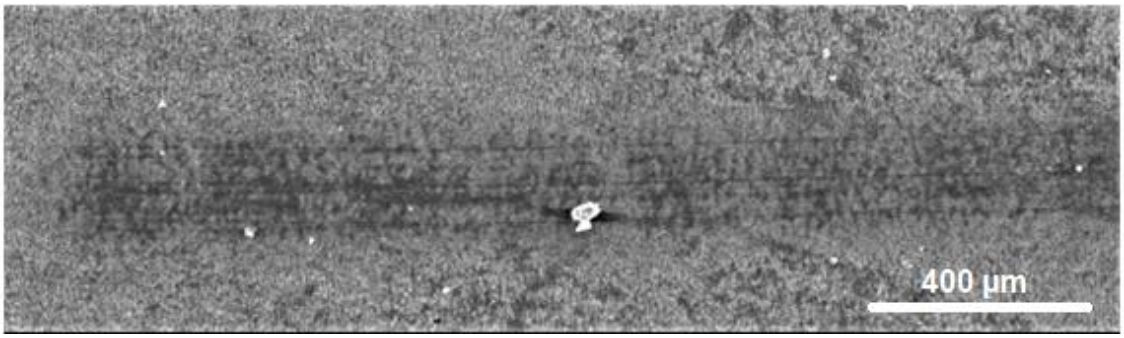

Figure 38 - Wear track obtained after 2000 cycles with 25 mN of the on the texturized surface with LIPSS, a parallel configuration.

Figure 39 (A to D) supports the previous claim. Figure 39 (A) and (B) show the SEM and oxygen map and allows us to see the oxide layer where on the top part, we have thinner but continuous film and a zone in the center of the track with oxides covering the LIPSS. Figure 39 (C) corresponds to an area with low oxide-film and low plastic deformation. Contrary to this, figure 39 (D) shows LIPSS covered with oxide film that suffers some plastic deformation. I attributed the formation of the continuous film to the increase in plastic deformation/contact area.

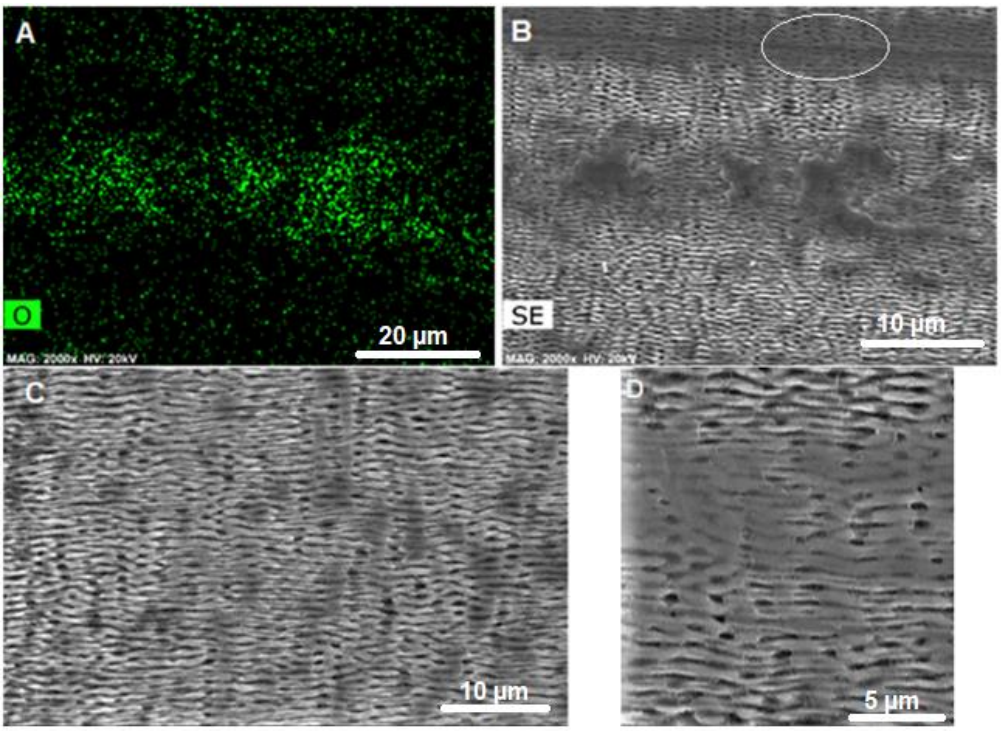

Figure 39 - Wear track obtained after 2000 cycles with 25 mN of the on the texturized surface with LIPSS, a parallel configuration. (A) oxygen map, (B,C,D) SEM images

4.6.2. Perpendicular alignment

Figure 40 displays the COF evolution for LIPSS during 2000 cycles, with perpendicular alignment and 10 and 25 mN load. By looking at the COF evolution, we immediately noticed that the behaviors are similar, and the 25 mN load tests attained the lowest COF.

The evolution of COF with 10 mN load and a perpendicular alignment allows us to see the first steady state regime until 400 cycles and a friction coefficient around 0.6. Next, there is a transition period between 400 and 550 cycles, leading to a higher second steady state regime with COF values between 0.8 and 0.9.

The 25 mN load run-in period corresponds to an increase in friction coefficient from 0.4 to 0.5, followed by the first steady state regime from 50 to 200 cycles. Finally, there is a transition period until achieving the second steady state regime with 0.7 μ.

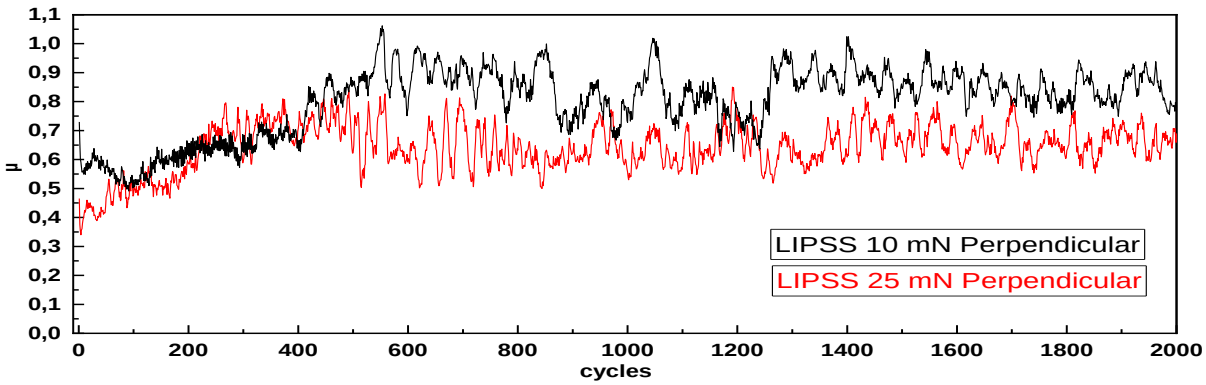

Figure 40 – Evolution of the friction coefficient during 2000 cycles with 10 and 25 mN loads of the LIPSS with perpendicular alignment.

The most notable things in figures 35 and 40 are: (I) the first 600 cycles the friction coefficient shows different behaviors for different alignments; (II) after the transition period, we can observe that throughout the 2000 cycles small and almost periodic increases and decreases in friction, Yu, Chengjiao [32] shows similar findings in his work[32] and attributed the trends observed in his work to the topography.

The performance in the perpendicular alignment is similar to the ones reported by Zhuo Wang [33] that states that the reduction in real contact area leads to a lower COF exhibited. Zhang, Dongya [40] attributes the decrease in friction coefficient to the so-called trapped effect, the ability to imprison nanoscale wear particles within the LIPSS channels, and to the shorter stiction length, measured in the perpendicular orientation on samples with narrow grooves.

If we look at figure 41 (A) and (B) that depicts the wear track for perpendicular alignment, the large tribo-layer surrounding the center contains small oxide zones and minor LIPSS deformation. Figure 41 (C), (D) shows a thicker oxide layer with two wear particles.

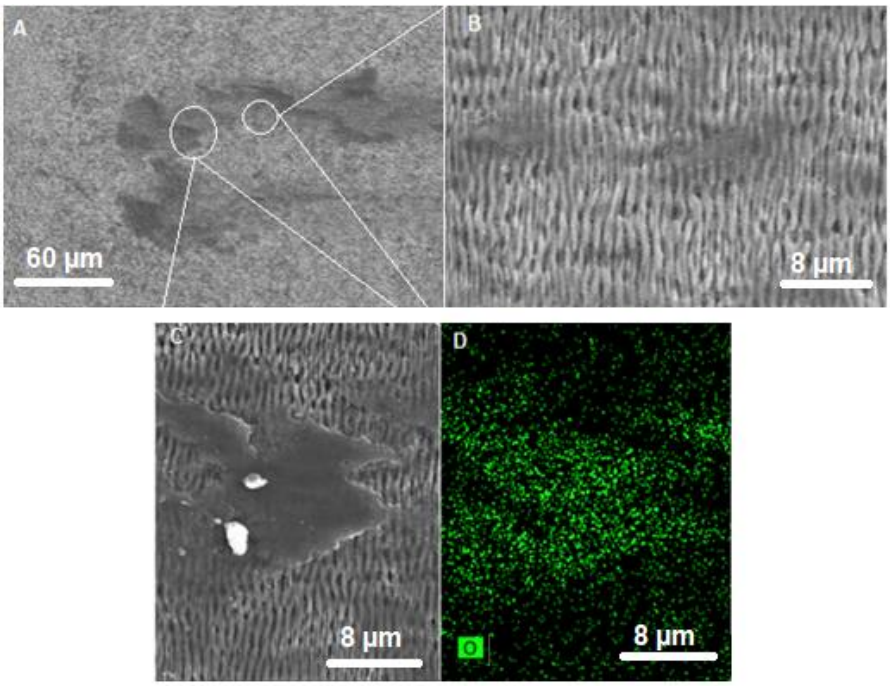

Figure 41 - Wear track obtained after 2000 cycles with 10 mN load of the textured surface with LIPSS with perpendicular alignment. (A), (B), (C) SEM images (D) Oxygen map.

Figure 42 (A), depicts the wear track with 25 mN load, shows the higher quantities of pushed oxide particles to the left side of the track. Figure 42 (B) shows a significant oxide region, and it is possible to see that on the top part of the figure, we have little damaged LIPSS, and on the bottom, we have LIPSS that suffered some plastic deformation.

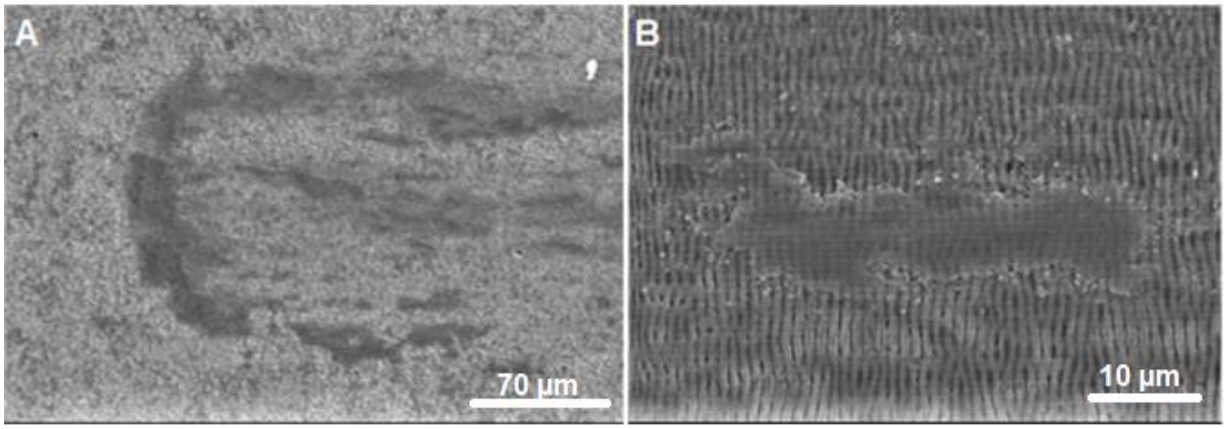

Figure 42 - Wear track obtained after 2000 cycles with 25 mN load of the textured surface with LIPSS perpendicular to the sliding direction.

.

Finally, figure 43 displays the SEM and oxygen map, where we see the thick oxide film that limits the left side of the track proving this way that the film on the surface is indeed oxide film.

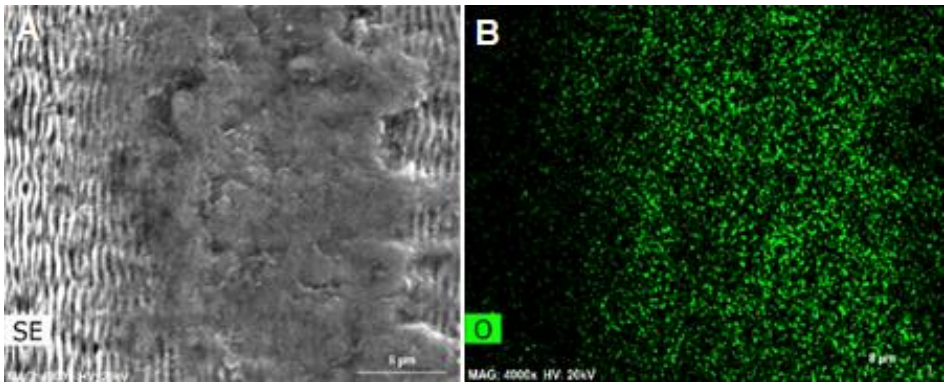

Figure 43 - SEM image of the oxide layer after 2000 cycles with 25 mN load of the LIPSS with perpendicular alignment. (A) SEM and (B) oxygen map.

4.7. Laser-induced periodic surfaces structures coated with graphene oxide

4.7.1. Parallel alignment

The friction coefficient evolution in LIPSS coated with GO during 2000 cycles with 10 and 25 mN for parallel alignment is exhibited in figure 44. They display similar behavior in the first 1200 cycles, where the 10 mN load track has an initial drop in COF from 0.6 to 0.4, followed by a steady state regime with a friction coefficient around 0.45 that persists until the end of the test. The 25 mN load evolution consists of a drop in friction from 0.65 to 0.55 and has the first steady state regime until 1200 cycles followed by a transition regime to the second plateau with a COF around 0.8.

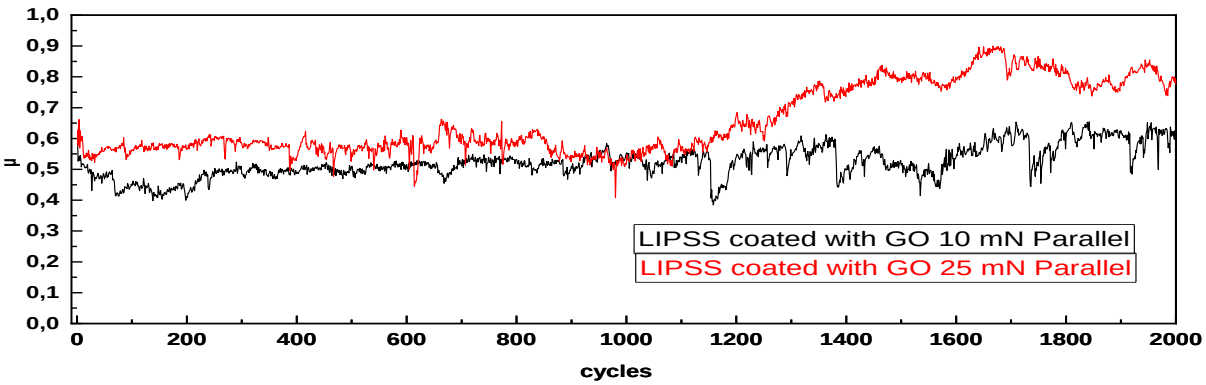

Figure 44 – Friction coefficient evolution during 2000 cycles with 10, and 25 mN loads of the LIPSS coated with GO and parallel alignment.

If we look at figure 45, we see a smooth coating of graphene oxide. We also observed two phenomena; (I) the presence of a hole/imperfection coated with GO; (II) Unlike the polished surface we did not attain wrinkles at the surface, and the GO appears to follow the LIPSS direction.

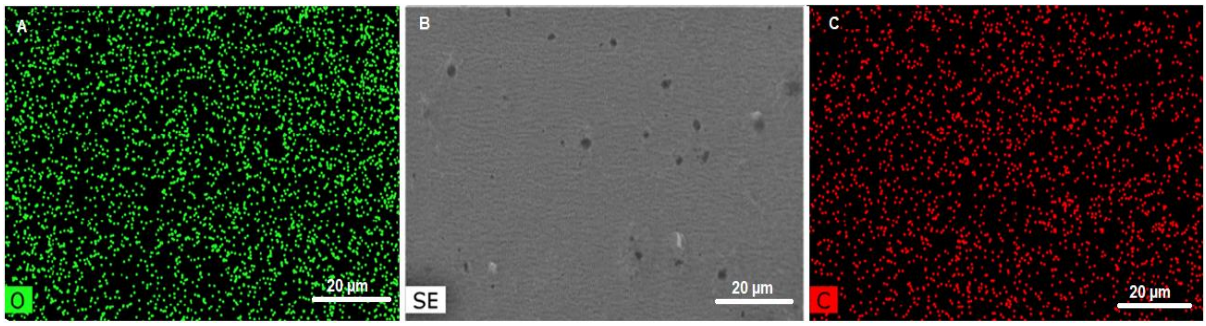

Figure 45 - SEM image and EDS map of the LIPSS coated with GO. (A) and (C) Oxygen and carbon map. (B) SEM image.

Once again, as described in[55][57], the track is limited by pushed GO. Figure 46 (A) show the 10 mN parallel alignment, where there is a higher concentration of GO on the left extremity. Analyzing figure 46 (B) and (C) allow us to see that after 2000 cycles the GO coating is still present on the surface. In figure 46 (B), similar to Xie[62], we observe a small crack on the film that is protecting the LIPSS and a zone with what appears to be undamaged LIPSS with peeled of GO. Finally, figure 46 (B) and (C) shows some small defects. In figure (B) we have, what appears to be, a hole coated with GO and in figure (C), we have a one hole with and a region with GO coating still intact where the surrounding LIPSS suffered some damage.

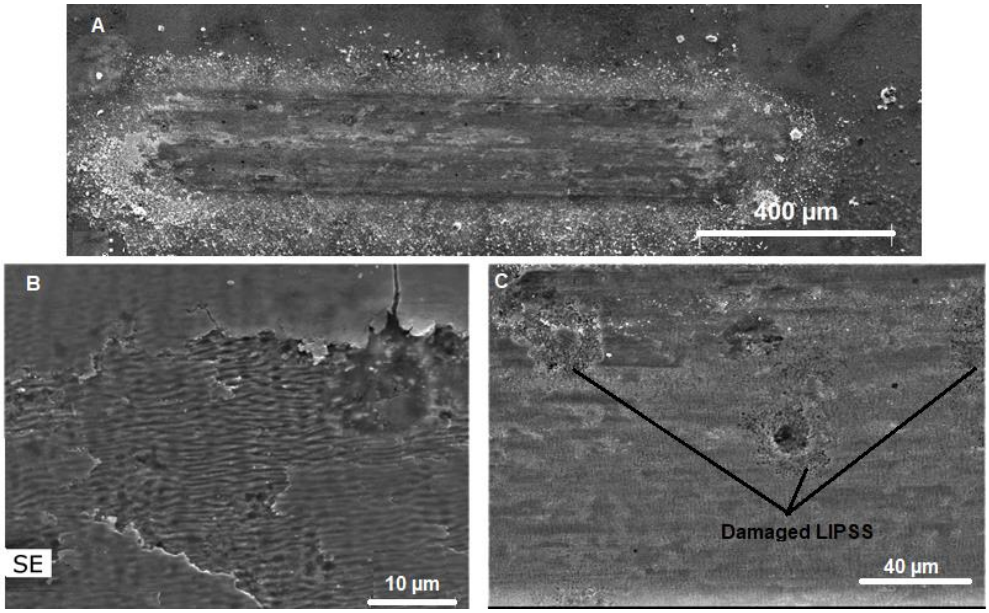

Figure 46 - Wear track obtained after 2000 cycles with 10 mN load of the LIPSS coated with GO parallel motion to LIPSS. (A), (B), (C) SEM images.

Looking at figure 47 (A) and (B) that displays the SEM images and EDS oxygen map for one defect coated with GO. The oxygen map shows what appears to be a large GO mass in the center and a lesser quantity of coating on the surrounding areas. Looking at both figures 45 and 47 (A-C), I assume that the small regions with a crack in the GO coating is a hole or depression filled with graphene oxide and after 2000 cycles the layer on top suffered damage and suffer some cracks.

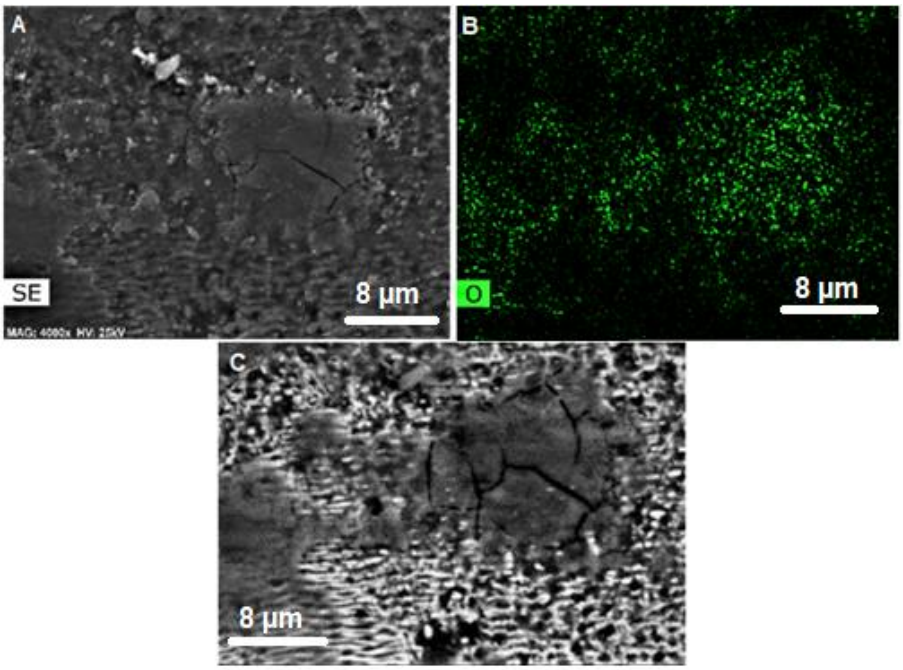

Figure 47 -Wear track obtained after 2000 cycles with 10 mN load of the LIPSS coated with GO for parallel configuration. (A) SEM image (B) Oxygen map, and (C) BSE image.

Figure 48 depicts the 25 mN load with parallel alignment. The track is restricted by pushed GO, where the highest concentration of GO occurs in the right extremity. Due to the radial distribution of the contact pressure been the maximum in the center formed a visible path (might have exposed LIPSS with little or no graphene oxide coat covering them explaining this way the friction behavior presented in figure 44.

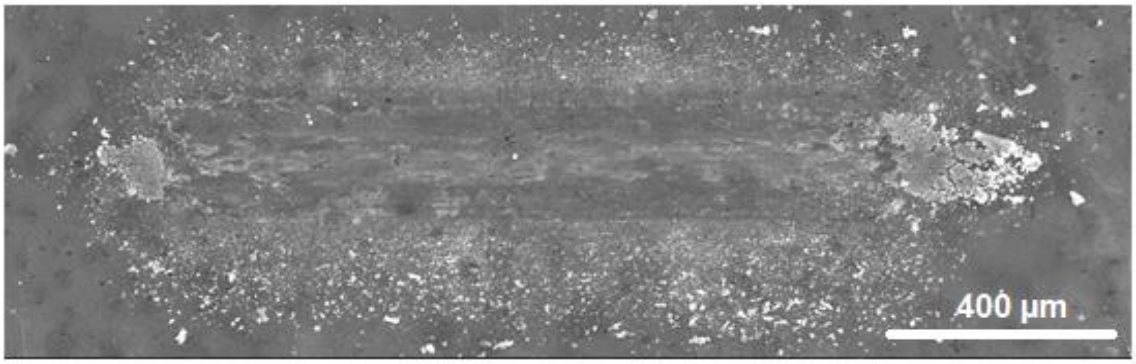

Figure 48 - Wear track obtained after 2000 cycles with 25 mN load of the LIPSS coated with GO for parallel alignment.

Figure 49 allows us to have a better understanding of the track where the oxygen map, figure 49 (B), shows us a considerable GO coating confining the wear track. Looking at figure 49 (C) shows a zone in the center that appears to have LIPSS with some plastic deformation.

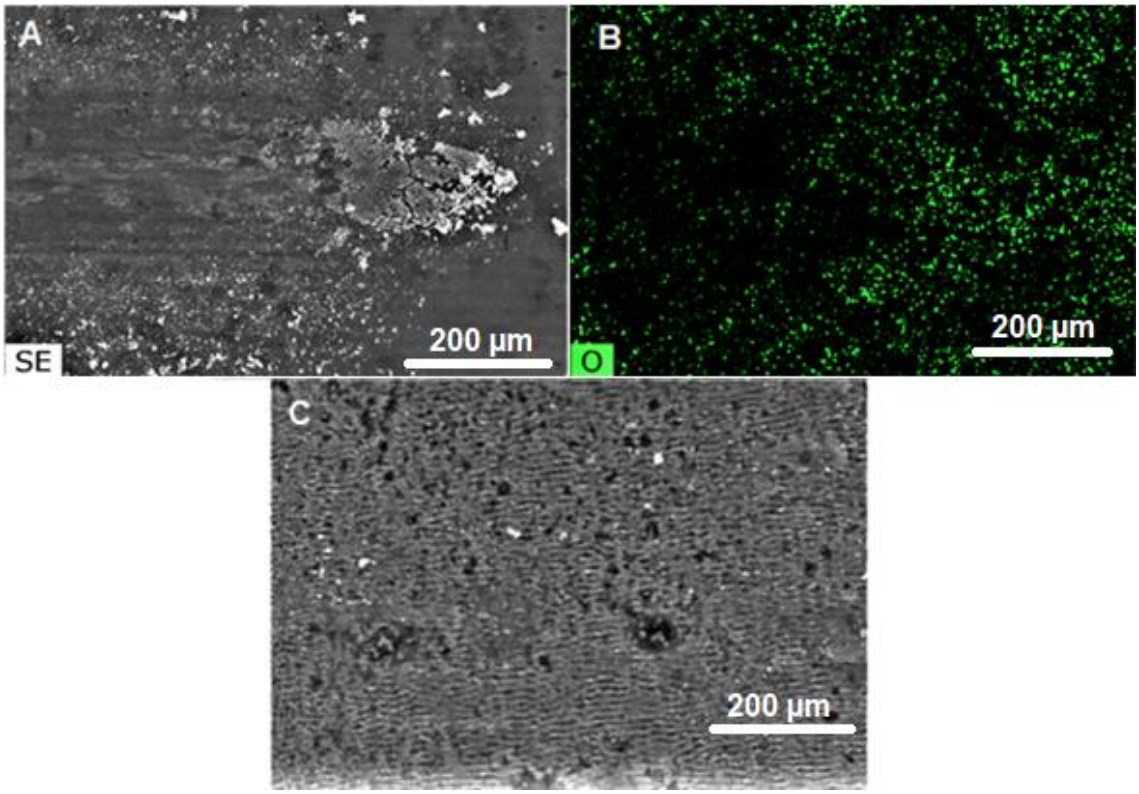

Figure 49 – Wear track obtained after 2000 cycles with 25 mN load of the LIPSS coated with GO for parallel alignment. (A) and (C) are SEM images, (B) oxygen maps.

4.7.2. Perpendicular alignment

Figure 50 depicts the friction coefficient evolution for LIPSS coated with GO during 2000 cycles, with 10 and 25 mN load, and perpendicular configuration. We are immediately captivated by the difference in behavior between the two loads. The 10 mN load has a stable steady state regime throughout the test. However, the 25 mN load shows a less stable and an increase in COF from 0.6 to 0.9 after 1100 cycles, achieving the second steady state regime.

The second most visible effect is the increase and erratic nature of the friction coefficient, (stick and slip)/oscillation behavior. Berman, Diana [58], displayed similar behavior in her work. She attributed this behavior to the removal of the lubricant from the surface after the initially protective period contact areas commence experiencing more and more metal to metal contact resulting in more wear.

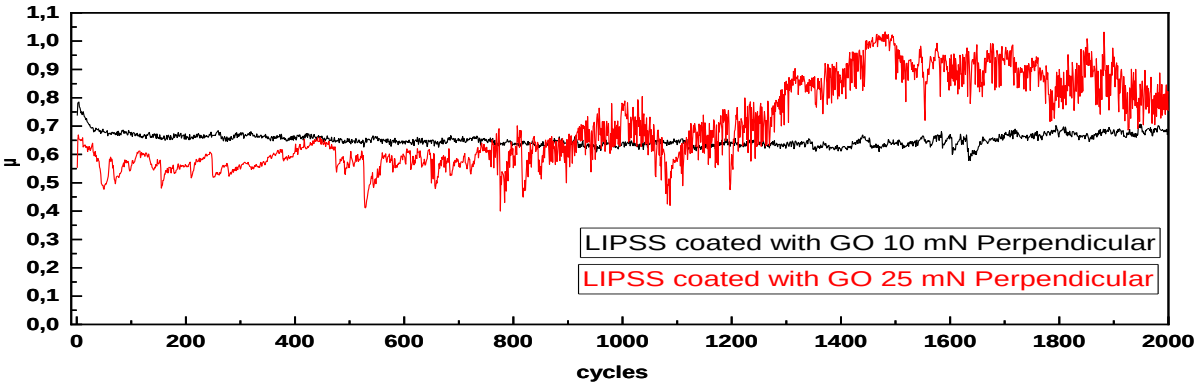

Figure 50 – Friction coefficient evolution during 2000 cycles with 10 and 25 mN loads of the LIPSS coated with GO for perpendicular alignment.

Looking at figure 51, the perpendicular alignment allows us to see that after 2000 cycles the GO coating was damaged but not destroyed. Figure 51 (A) shows one similarity to the parallel configuration, the inner path attained in the center of the track. The path is what I assume exposed LIPSS, similar to the one in figure 48. The SEM images and oxygen map displayed in figure 51 (C) and (D) show that on the top part of the path a GO layer that covers and protects the LIPSS. Also, the exposed LIPSS appear to have little or no plastic deformation and we can see two GO particles, that are caused by agglomeration of GO during the test.

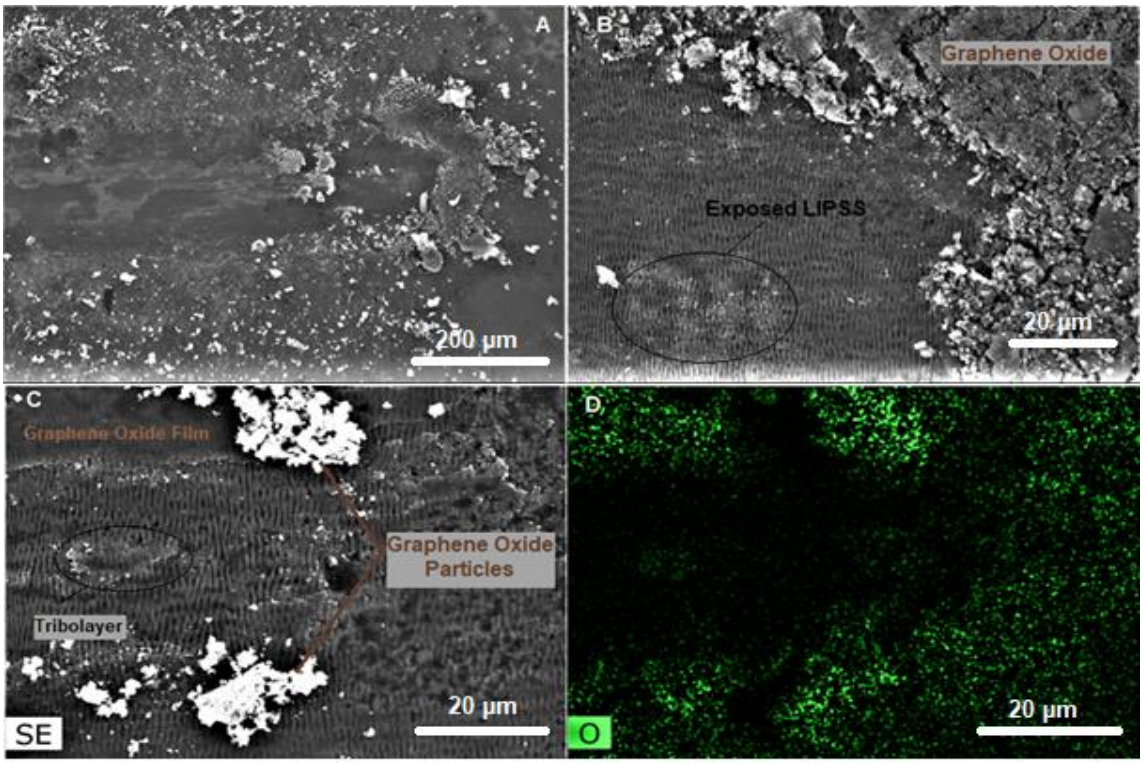

Figure 51 - Wear track obtained after 2000 cycles with 10 mN load of the LIPSS coated with GO for perpendicular alignment. (A), (B) and (C) are SEM image (D) Oxygen map.

Figure 52 shows the Wear track obtained after 2000 cycles in LIPSS coated with graphene oxide, perpendicular alignment, and 25 mN load. We see an inner path in the center of the track that is associated with the interaction between surfaces and radial distribution.

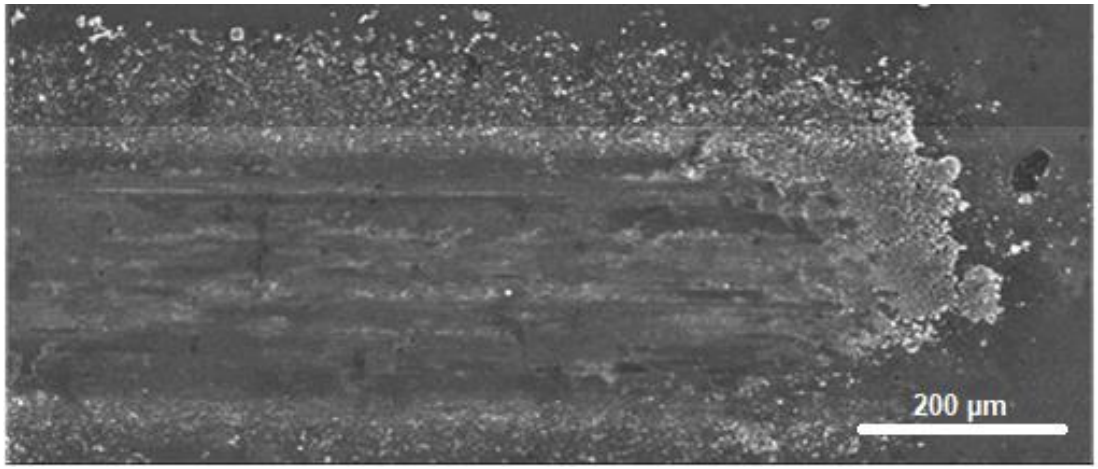

Figure 52 - Wear track obtained after 2000 cycles with 25 mN load of the LIPSS coated with graphene oxide for perpendicular alignment, and.

.

Looking at figure 53 SEM images for 25 mN perpendicular configuration, allows us to understand the difference in friction performance by showing evidence that supports oscillations similar to stick and slip phenomenon. However, LIPSS reduced the contact area and making the adhesion wear almost impossible to occur without seeing severe plastic deformation. Similar to our previous hypothesis Berman, Diana [57], and Zheng, Dan [59] also attained an unstable COF behavior in their works.

Figure 53 (A) and (B) support the claim that even after 2000 cycles there is a GO coating that covers and protects the LIPSS from any damage and also can see a crack film similar to Xie, Hongmei.[63] In addition, figure 52 (C) and (D) show a region with an oxide film that cover the LIPSS and where we see LIPSS without much plastic deformation.

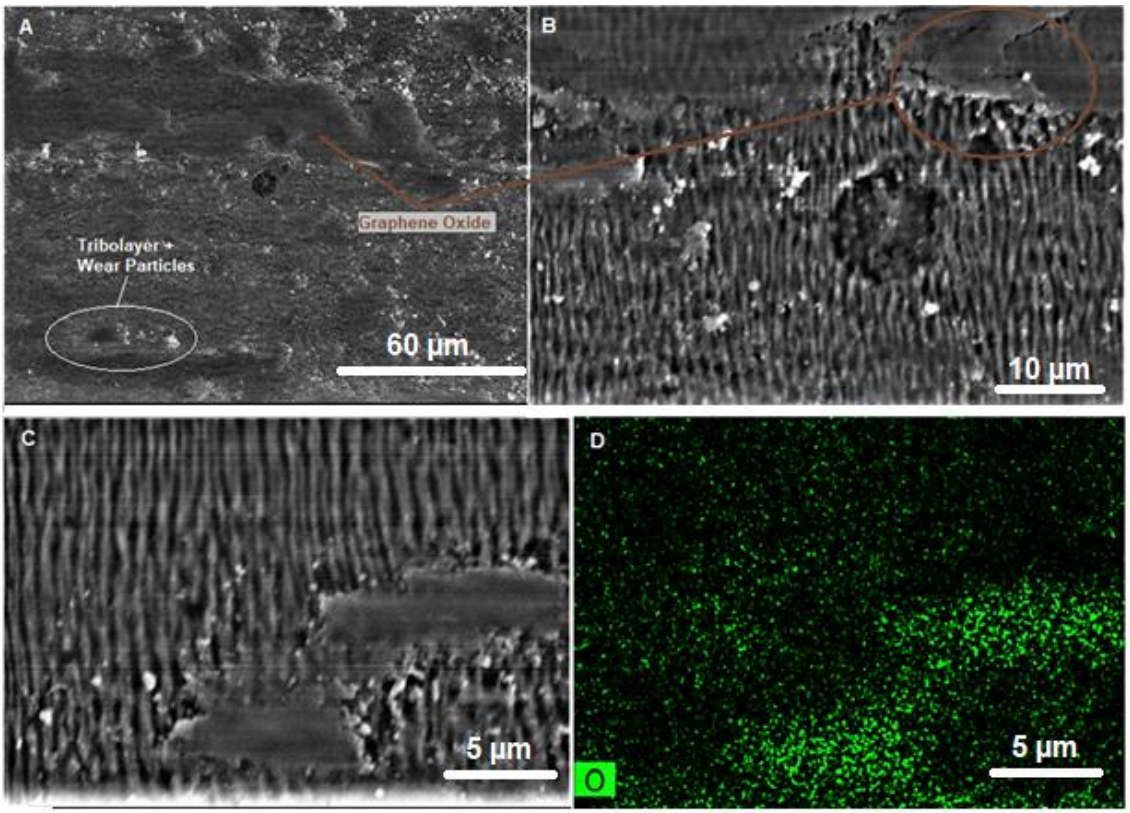

Figure 53 – SEM images for wear track obtained after 2000 cycles with 25 mN load of the LIPSS coated with GO for perpendicular to the sliding motion. (A), (B), (C) are SEM images, (D) oxygen map.

4.1. Laser-induced periodic surfaces structures coated with graphene

4.1.1. Parallel alignment

Figure 54 represents friction coefficient evolution during 5000 cycles on LIPSS coated with Gr with the parallel configuration for 10 and 25 mN loads. The COF evolution for 10 mN loads and parallel alignment consists of a run-in period with a drop in COF from 0.55 to [0.3; 0.4] followed by a steady state regime that goes until the end of the test. The 25 mN load exhibits a steady state plateau with a friction coefficient of around 0.55.

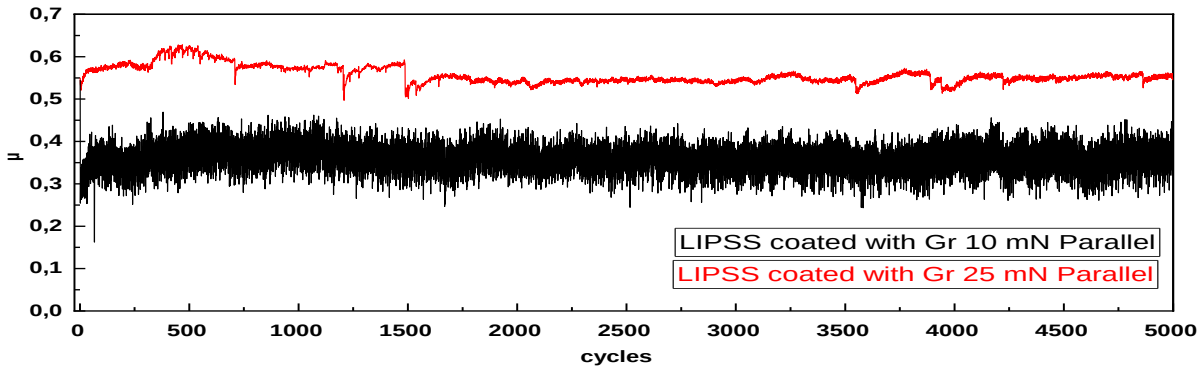

Figure 54 – Friction coefficient evolution after 5000 cycles with 10 and 25 mN loads of the LIPSS coated with Gr for parallel configuration, 10 and 25 mN loads.

The phenomenon that we immediately perceive is the oscillation present in 10 mN load. The behavior is similar to the ones attained in figure 27 for polished surfaces coated with graphene. Ismail, Nurul Athirah.[61] also showed analogous oscillation in his work.

Looking at figure 55, we can see LIPSS coated with graphene, and in figure (A), we observe a coating with some almost spherical particles that correspond to Gr agglomerations.

The two possible formation systems for this behavior are: (I) graphene dispersion was not the best before the droplet atomization process. The other could be that the deposited Gr stack layers to the surface can break. This phenomenon coupled with the wettability properties of the coating promotes agglomeration and creates large Gr particles seen in figure 55.

Figures 55 (B) and (C) are the carbon and oxygen maps that show a carbon layer (graphene) completely covering the LIPSS. Figure (D) shows that our initial assumption about how graphene connects with LIPSS was right.

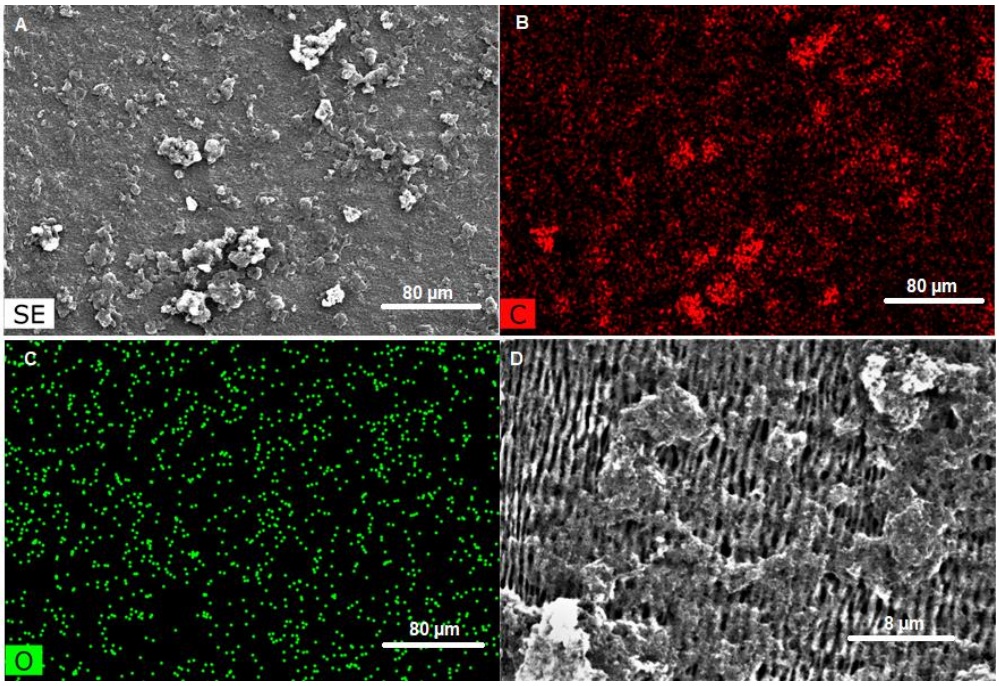

Figure 55 - Wear track obtained after 5000 cycles of the LIPSS coated with graphene. (A) and (D) are SEM image, (B) and (C) carbon and oxygen maps.

Observing figure 56 (A), (B), we see that Gr coating was pushed to the sides and has similar darker graphene zones to the ones attained in figure 29. The wear track has three different zones; (I) the Gr coating was damaged or pushed to the sides exposing the LIPSS, (II) the top and bottom part of the wear track appear to have a surface with a smoother look. On the boundaries, we have darker areas that I assume to be created by Gr agglomeration or compressed graphene. Finally, we have a graphene zone surrounding the wear track that corresponds to undamaged or untouched graphene, similar to figure 55.

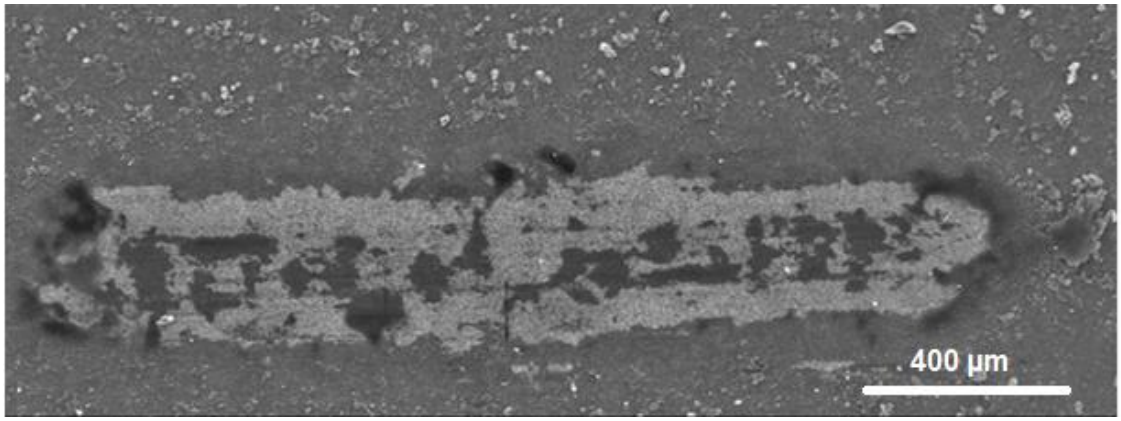

Figure 56 - Wear track obtained after 5000 cycles with 10 mN load of the LIPSS coated with Gr, for parallel alignment.

Figure 57 (A) confirms that the LIPSS did not suffer any plastic deformation. The small grey areas located in the center of the track are indeed graphene spots. If we look at figure 57 (B), we observe that the dark areas around the track consist of pushed and compressed Gr caused by the periphery of the sphere.

.

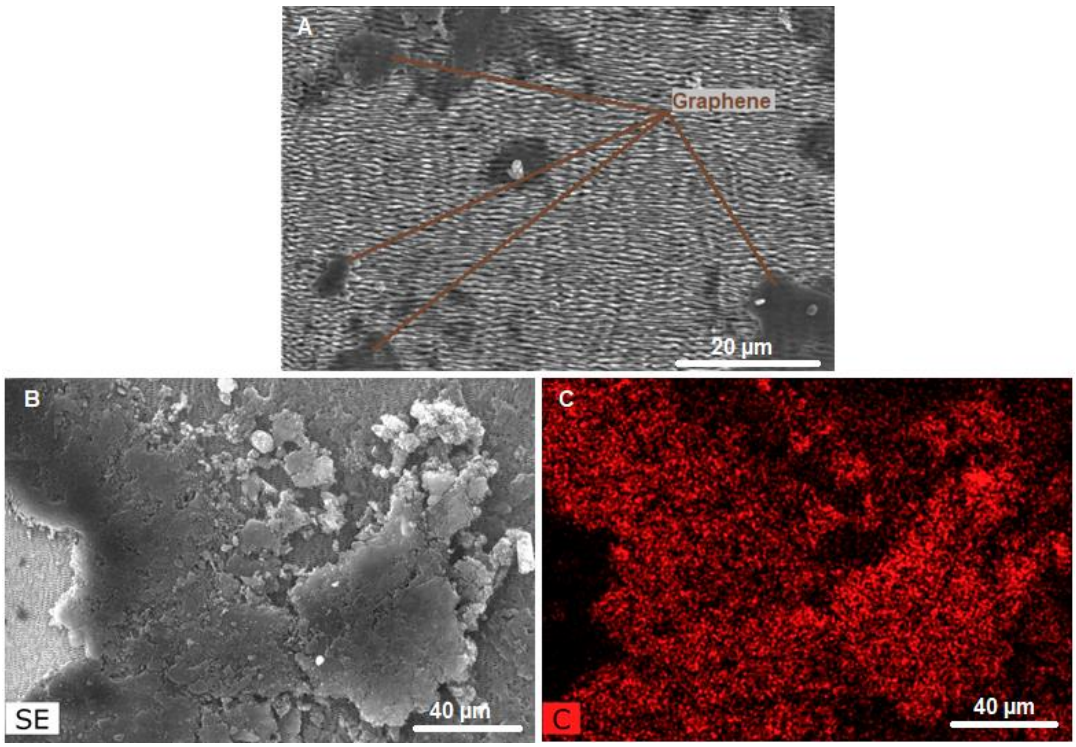

Figure 57 - Wear track obtained after 5000 cycles with 10 mN load of the LIPSS coated with Gr, a parallel alignment. (A) and (B) are SEM image, (C) carbon map.

Figure 56 and 58 show a similar track. The only difference is the Gr in the middle of the track appears to be in higher quantities.

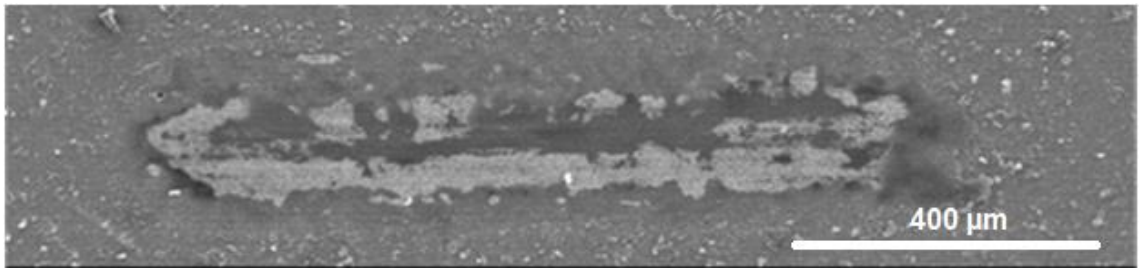

Figure 58 - Wear track obtained after 5000 cycles with 25 mN load of the LIPSS coated with Gr for parallel alignment.

It's possible to see a higher accumulation of GR at the right side of the track consistent with what we have seen before. The Gr coating that remained on the surface has a lower thickness, similar to the parallel 10 mN test. Looking closely at figure 59, we observe that the LIPSS did not suffer any damage even after 5000 cycles and we can confirm that the area in the center of the track is indeed graphene.

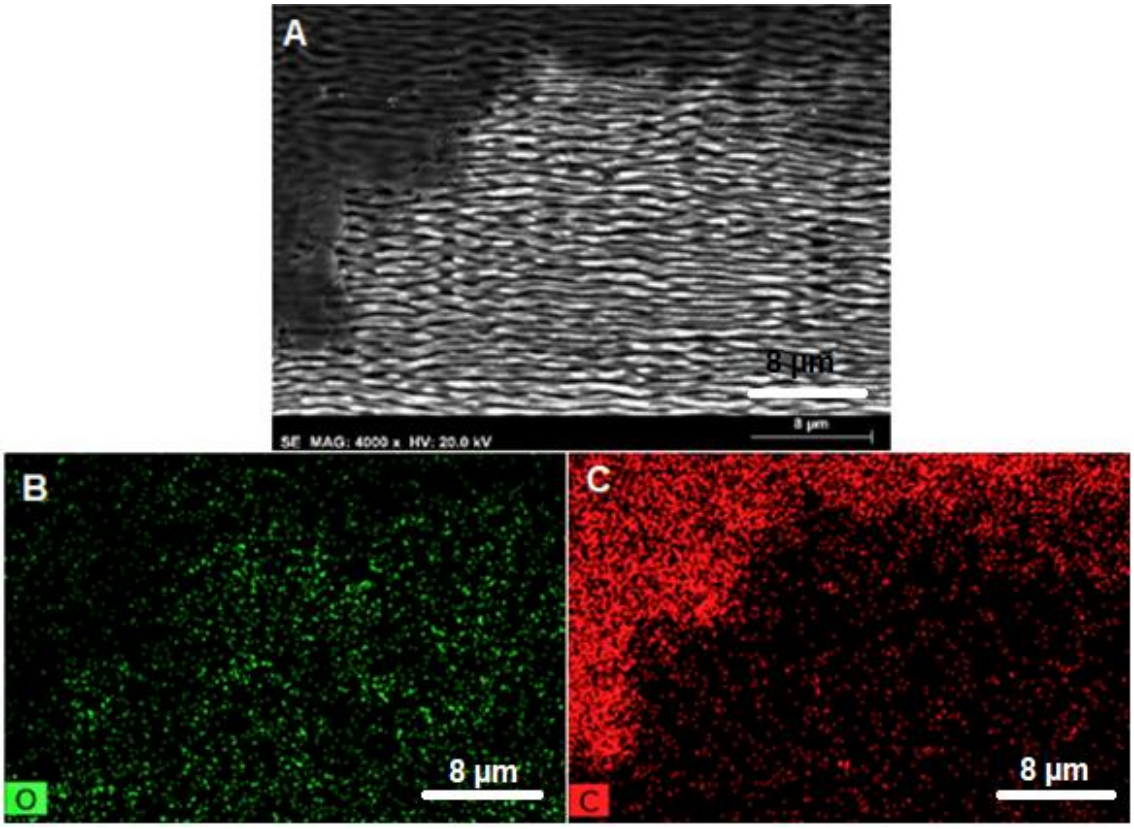

Figure 59 - wear track obtained after 5000 cycles with 25 mN load of the LIPSS coated with Gr for parallel configuration. (A) are an SEM image (B) and (C) oxygen and carbon map, respectively.

4.1.2. Perpendicular alignment

Looking at figure 59 that shows the evolution of COF with 10 and 25 mN and perpendicular alignment, we observe that the 10 mN load test has a different behavior from 25 mN load. This progress consists of continuous growth until the end of the test. The 25 mN load is similar to other tests and is a steady state regime throughout the 5000 cycles.

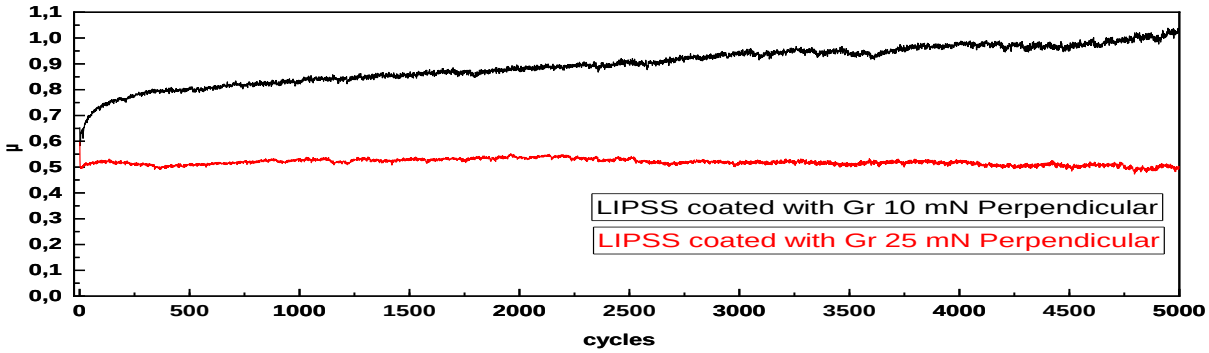

Figure 60 - Friction coefficient evolution during 5000 cycles with 10 and 25 mN loads of the LIPSS coated with Gr for parallel configuration.

Figures 61 shows a completely different track from the ones presented before. We have almost no exposed LIPSS, and large quantities of what I assume is Gr and oxide layer covering the LIPSS. This assumption supports the strange behavior seen in the respective COF growth.

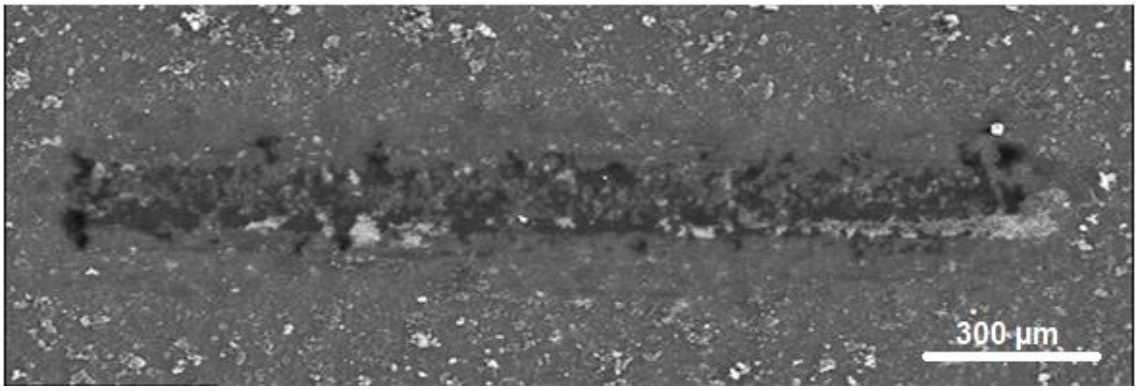

Figure 61 - Wear track obtained after 5000 cycles with 10 mN load of the LIPSS coated with Gr for perpendicular alignment.

Figure 62 shows several images of the 10 mN load tracks, (A) SEM and (B), (C) are carbon and oxygen images, respectively. They discredit our previous assumption, the majority of the layer that covers the surface throughout the track is just graphene. Looking at the oxygen map, we see a higher concentration of oxides in the exposed LIPSS zone. If we look at figure 62 (A) and (D), we observe a solid graphene coating that caused the interaction between the sphere and this solid Gr coating that lead to the increase in COF.

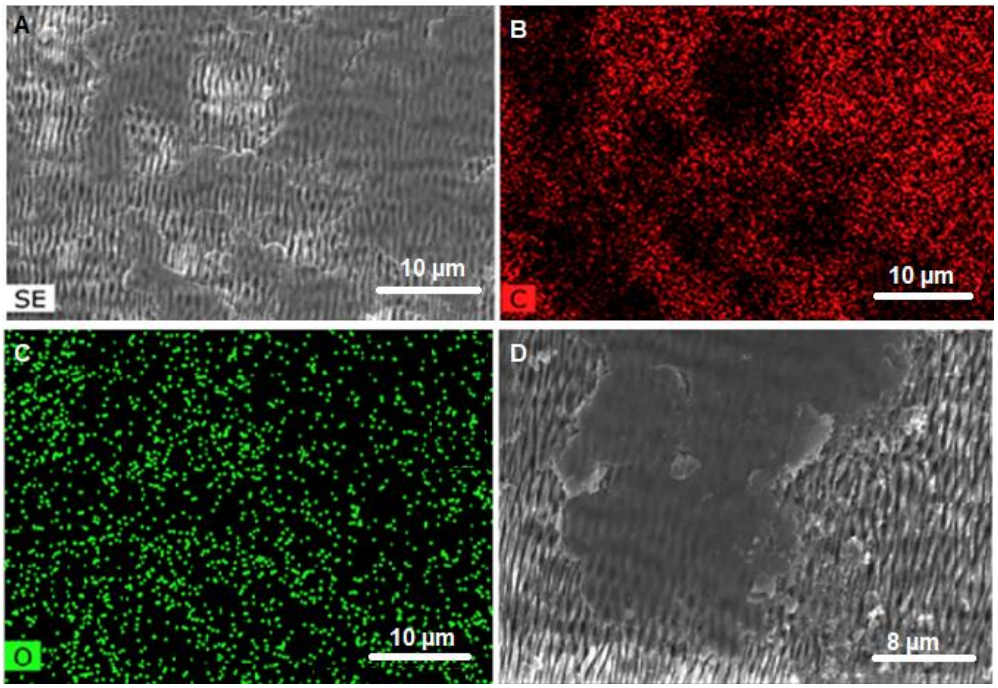

Figure 62 - Wear track obtained after 5000 cycles with 10 mN load of the LIPSS coated with Gr for perpendicular alignment. (A) is an SEM image (B) and (C) are Carbon and oxygen map.

If we look at figure 63, we observed a behavior like the previous ones (except 10 mN perpendicular). The only difference is the graphene layer covers the lower part of the track.

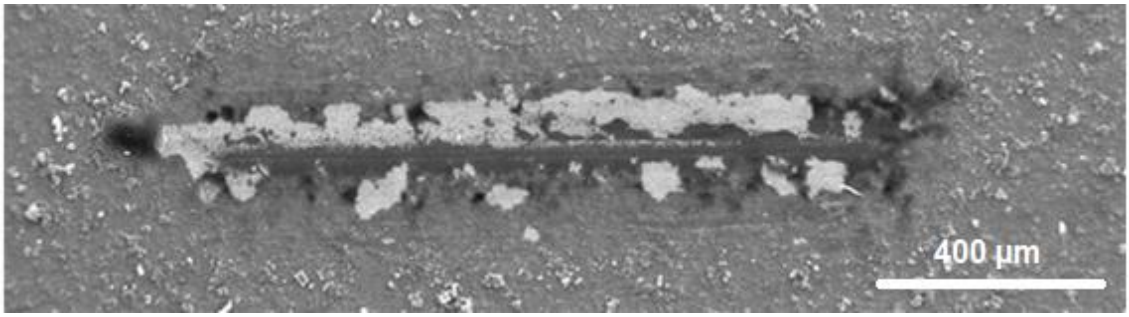

Figure 63 - Wear track obtained after 5000 cycles with 25 mN load of the LIPSS coated with Gr for perpendicular alignment.

Taking a closer look at the center of the track, figure 64, allows us to see two distinctive Gr zones. Figure 64 (A) appears to have a small damage Gr film with Gr grains surrounding it. Figure 64 (B) shows a thinner film that resembles peel off graphene. Figure (C) and (D) is the oxygen and carbon maps that show oxides present where the LIPSS are exposed and that the Gr layer provides protection to the LIPSS.

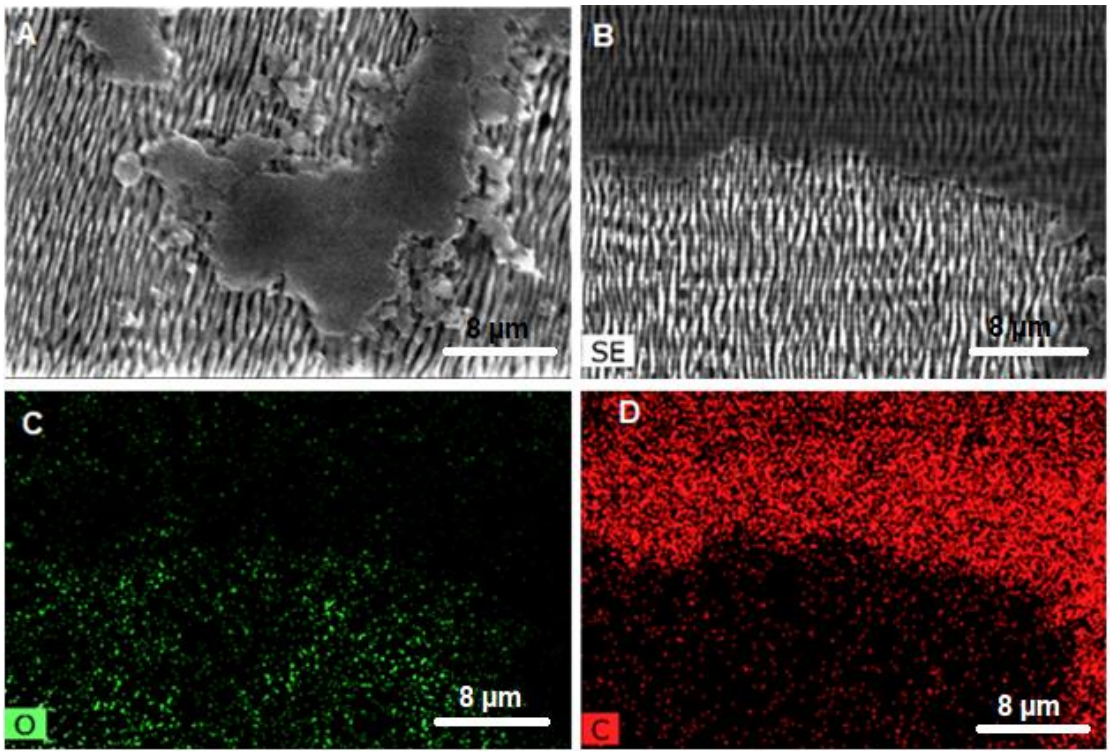

Figure 64 - (A) and (B) wear track obtained after 2000 cycles with 25 mN load of the LIPSS coated with graphene for perpendicular alignment. (B) oxygen map.

4.2. Work summary

Comparing all friction coefficient evolutions for polished and textured surfaces with and without GO or Gr coatings allows us to state that the introduction of laser-induced periodic structures reduce the COF observed.

We also see a considerable reduction in friction coefficient when we coated both polished and LIPSS with GO and Gr solid lubricant, showing this way that LIPSS on tool steel can act as reservoirs for graphene-based lubricant.

In our work, we observed the lowest friction coefficient in LIPSS coated with graphene 10 mN load and parallel alignment and polished surface with 20 mN load. However, unlike the results of Xiei[63] the present study showed that Gr as lubricant results in a lower COF when compared with that obtained for GO coatings.

5. Conclusions and future work

The objective of this work is to study the influence of graphene-base solid lubricant. We evaluated the evolution of the friction coefficient for lubricated and unlubricated conditions and polished and textured surfaces with LIPSS in tool steel.

We need to have into consideration that graphene oxide and graphene had different concentrations and layers. This parameter can have a tremendous influence on friction and wear. Since both graphene lubricants have different concentrations and layers, we will not compare the results in terms of coating strength.

The friction coefficients values were measured with different types of surface finishes: (i) polished, (ii) laser textured surface (LIPSS), and (iii) both coated with graphene-oxide and graphene. Surface texturing carried out under the same conditions that lead to the formation of LIPSS (“Laser-Induced Periodic Surface Structures”) previously done by Ana Beatriz Ferreira. In the samples textured by laser, tests were carried out in the perpendicular and parallel sliding direction to the LIPSS to establish the effect of the orientation on the tribological behavior.

The final friction coefficient values obtained for dry sliding are well in range with the ones established in the literature. However, in LIPSS there is not much information available. In addition, the LIPSS that we attained have different characteristics, depth, and the contact area, so further analyses may be necessary.

Another task in this work was the assessment of deposition methods for graphene-based lubricant. After some small tests and studies, the method chosen was sprayed deposition. We chose this method

because of two factors: (i) the graphene oxide and graphene layer created were the most homogeneous, (ii) the reproducibility of the layer in different samples.

The difficulties that I got in this method were (I) graphene needed to be better dispersed to avoid agglomeration where the flake cluster will generate lower adherence to the surface and layer; (II) no control over deposition thickness; (III) creating a uniform or homogenous graphene coating.

I believe that graphene lubricant coating can improve if we have a more dispersed solution, or if better deposition equipment is employed.

The above conclusions mean that it is required to perform a study about airbrush deposition methods where we control parameters such as distance between sample and airbrush, the temperature of the air, surface tension, nozzle pressure ratio between Gr and air, etc.

In this work, we were able to reduce the friction coefficient by introducing LIPSS into a surface. Gr coating generated a better friction coefficient as a solid lubricant than GO. Analyzing the GO performance, we observed that they have similar friction coefficient values independent of the surface treatment. Nevertheless, we cannot ignore that textured surfaces with LIPSS act as a lubricant reservoir for GO coatings and were able to increase the coating lifetime.

Finally, we scrutinize graphene as a solid lubricant for both perpendicular and parallel alignments and loads. We notice two main effects; (I) the typical friction curve is not achieved, which means more tests with a higher amount of cycles are necessary; (II) the sliding motion parallel to the LIPSS has the lowest friction coefficient observed, between [0.3; 0.4]. Attained in a surface with LIPSS parallel alignment 10, and 25 mN polished with graphene lubricant

The most obvious conclusions are that we were able to reduce the friction coefficient by introducing LIPSS into a surface and introducing GO or Gr as solid lubricants produce a higher reduction in friction coefficient and friction stability. Finally, we observed that graphene has a better friction coefficient as a solid lubricant then GO.

With this in mind, it is necessary to obtain more information, better understanding, and description for certain behaviors: (i) values of friction coefficient obtained in some GO test, (ii) the lubricant layer lifetime, (iii) stick and slip phenomenon, etc. As already explained, many different parameters influence the performance of the friction coefficient, so it is necessary to comprehend the main differences to fully identify which lubricant is better or in what condition is better.

When looking at layer lifetime influenced by the deposition method, it is necessary to perform more tests in order to fully understand what causes the differences between layer thickness, imperfections and better understand the interaction between coating and matrix.

Future work requires a deeper analysis of mechanisms that are behind friction in LIPSS and graphene-based solid lubricants. These are some ideas that are alluring to try in order to understand and prove the usage of said systems.

After this small study, we can say for sure that there is a requirement for the continuation of our work and perform different tests. i.e. the increase in load, preparation, and analysis of better/different graphene dispersion, a study about Gr concentration, development of the same test but using GO powder similar to Gr, improve LIPSS in order to have better reservoir capability, increase the number of cycles and study the influence of velocity will alter the friction coefficient.

References

[1] V. L. Popov, “Is Tribology Approaching Its Golden Age? Grand Challenges in Engineering Education and Tribological Research,” *Front. Mech. Eng.*, vol. 4, no. November, pp. 1–6, 2018.

[2] J. M. Romano, A. Garcia-Giron, P. Penchev, and S. Dimov, “Triangular laser-induced submicron textures for functionalising stainless steel surfaces,” *Appl. Surf. Sci.*, vol. 440, pp. 162–169, 2018.

[3] F. Fraggelakis, G. Mincuzzi, J. Lopez, I. Manek-Hönninger, and R. Kling, “Controlling 2D laser nano structuring over large area with double femtosecond pulses,” *Appl. Surf. Sci.*, vol. 470, no. November 2018, pp. 677–686, 2019.

[4] A. Peter, A. H. A. Lutey, S. Faas, L. Romoli, V. Onuseit, and T. Graf, “Direct laser interference patterning of stainless steel by ultrashort pulses for antibacterial surfaces,” *Opt. Laser Technol.*, vol. 123, no. November, p. 105954, 2020.

[5] A. Beatriz, “Comportamento Tribológico de Superfícies Metálicas Nanotexturadas com Lasers de Femtosegundo,” Instituto Superior Técnico, 2017.

[6] J. Bonse, S. V. Kirner, M. Griepentrog, D. Spaltmann, and J. Krüger, “Femtosecond laser texturing of surfaces for tribological applications,” *Materials (Basel).*, vol. 11, no. 5, p. 801, 2018.

[7] K. Holmberg and A. Erdemir, “Global impact of friction on energy consumption, economy and environment,” *FME Trans.*, vol. 43, no. 3, pp. 181–185, 2015.

[8] K. Holmberg and A. Erdemir, “Influence of tribology on global energy consumption, costs and emissions,” *Friction*, vol. 5, no. 3. pp. 263–284, 2017.

[9] M. S. Singh, “Lubricants Market worth $188.0 billion by 2024,” *MarketsandMarkets™ INC.*, 2019. [Online]. Available: https://www.marketsandmarkets.com/PressReleases/lubricants-market.asp. [Accessed: 13-Apr-2020].

[10] G. view Research, “Lubricants Market Size Worth $167.5 Billion By 2027,” *May*, 2020. [Online]. Available: https://www.grandviewresearch.com/press-release/global-lubricants-market. [Accessed: 10-Aug-2020].

[11] M. & F. Chemicals, “Graphite Lubricant Market, By Application (Solution, Pure Powder, and composites), By End-user (Transportation, Industrial Application, and Electrical & Electronics) and By Geography – Drivers, Restraints, Opportunities, Trends and Forecast up to 2022,” *August*, 2017. [Online]. Available: https://www.infoholicresearch.com/report/graphite-lubricant-market-global-drivers-opportunities-trends-and-forecast-up-to-2022/.

[12] Bharat Bhushan, *MODERNN HANDBOOK TRIBOLOGY Principles of Tribology*. 2001.

[13] I. Hutchings and P. Shipway, “Tribology: Friction and wear of engineering materials: Second Edition.” pp. 1–388, 2017.

[14] K. C. Ludena and Oy. O. Ajayi, “Friction, Wear, Lubrication,” *Foreign Affairs*, vol. 9, no. 5. pp. 1–294, 2018.

[15] J. A. Norris, K. J. Stabile, and R. H. Jinnah, “An introduction to tribology.,” *Journal of surgical orthopaedic advances*, vol. 17, no. 1. pp. 2–5, 2008.

[16] A. Cunha, “Multiscale Femtosecond Laser Surface Texturing of Titanium and Titanium Alloys for Dental and Orthopaedic Implants,” Instituto Superior Técnico, 2015.

[17] A. Beltaos *et al.*, “Femtosecond laser induced periodic surface structures on multi-layer graphene,” *J. Appl. Phys.*, vol. 116, no. 20, pp. 1–6, 2014.

[18] R. Stefan, F. Preusch, and H. Ralf, “Generation of Low-Spatial Frequency Laser Induced Periodic Surface Structures Driven by Surface Finish,” vol. 10, pp. 1–8, 2015.

[19] M. Birnbaum, “Semiconductor surface damage produced by Ruby lasers,” *J. Appl. Phys.*, vol. 36, no. 11, pp. 3688–3689, 1965.

[20] A. E. Siegman and P. M. Fauchet, “Stimulated Wood’s Anomalies on Laser-Illuminated Surfaces,” *IEEE J. Quantum Electron.*, vol. 22, no. 8, pp. 1384–1403, 1986.

[21] J. J. Yu and Y. F. Lu, “Laser-induced ripple structures on Ni-P substrates,” *Appl. Surf. Sci.*, vol. 148, no. 3, pp. 248–252, 1999.

[22] A. Y. Vorobyev and C. Guo, “Direct femtosecond laser surface nano/microstructuring and its applications,” *Laser Photonics Rev.*, vol. 7, no. 3, pp. 385–407, 2013.

[23] A. Mizuno, T. Honda, J. Kikuchi, Y. Iwai, N. Yasumaru, and K. Miyazaki, “Friction Properties of the DLC Film with Periodic Structures in Nano-scale,” *Tribol. Online*, vol. 1, no. 2, pp. 44–48, 2006.

[24] N. Yasumaru, K. Miyazaki, and J. Kiuchi, “Control of tribological properties of diamond-like carbon films with femtosecond-laser-induced nanostructuring,” *Appl. Surf. Sci.*, vol. 254, no. 8, pp. 2364–2368, 2008.

[25] A. Rosenkranz, L. Reinert, C. Gachot, and F. Mücklich, “Alignment and wear debris effects between laser-patterned steel surfaces under dry sliding conditions,” *Wear*, vol. 318, no. 1–2, pp. 49–61, 2014.

[26] I. Gnilitskyi *et al.*, “Nano patterning of AISI 316L stainless steel with Nonlinear Laser Lithography: Sliding under dry and oil-lubricated conditions,” *Tribol. Int.*, vol. 99, pp. 67–76, 2016.

[27] J. Bonse *et al.*, “Tribological performance of femtosecond laser-induced periodic surface structures on titanium and a high toughness bearing steel,” in *Applied Surface Science*, 2015,

vol. 336, pp. 21–27.

[28] J. Bonse, S. V. Kirner, R. Koter, S. Pentzien, D. Spaltmann, and J. Krüger, “Femtosecond laser-induced periodic surface structures on titanium nitride coatings for tribological applications,” *Appl. Surf. Sci.*, vol. 418, pp. 572–579, 2017.

[29] I. Alves-Lopes, A. Almeida, V. Oliveira, and R. Vilar, “Influence of laser surface nanotexturing on the friction behaviour of the silicon/sapphire system,” *Opt. Laser Technol.*, vol. 121, no. July 2019, p. 105767, 2020.

[30] I. Alves-Lopes, A. Almeida, V. Oliveira, and R. Vilar, “Influence of femtosecond laser surface nanotexturing on the friction behavior of silicon sliding against ptfe,” *Nanomaterials*, vol. 9, no. 9, 2019.

[31] G. S. Joshi *et al.*, “Effects of the micro surface texturing in lubricated non-conformal point contacts,” *Tribol. Int.*, vol. 127, no. November 2017, pp. 296–301, 2018.

[32] C. Yu and Q. J. Wang, “Friction anisotropy with respect to topographic orientation,” *Sci. Rep.*, vol. 2, pp. 1–6, 2012.

[33] Z. Wang, Q. Zhao, and C. Wang, “Reduction of friction of metals using laser-induced periodic surface nanostructures,” *Micromachines*, vol. 6, no. 11, pp. 1606–1616, 2015.

[34] Z. Wang, Q. Zhao, C. Wang, and Y. Zhang, “Modulation of dry tribological property of stainless steel by femtosecond laser surface texturing,” *Appl. Phys. A Mater. Sci. Process.*, vol. 119, no. 3, pp. 1155–1163, 2015.

[35] C. Yu, H. Yu, G. Liu, W. Chen, B. He, and Q. J. Wang, “Understanding topographic dependence of friction with micro- and nano-grooved surfaces,” *Tribol. Lett.*, vol. 53, no. 1, pp. 145–156, 2014.

[36] B. He, W. Chen, and Q. Jane Wang, “Surface texture effect on friction of a microtextured poly(dimethylsiloxane) (PDMS),” *Tribol. Lett.*, vol. 31, no. 3, pp. 187–197, 2008.

[37] D. B. HAMILTO, J. A. WALOWI, and C. M. ALLEN, “A theory of lubrication by micro irregularities,” *Wear*, vol. 10, no. 5, p. 412, 1967.

[38] M. Geiger, S. Roth, and W. Becker, “Influence of laser-produced microstructures on the tribological behaviour of ceramics,” *Surf. Coatings Technol.*, vol. 100–101, no. 1–3, pp. 17–22, 1998.

[39] S. V. Kirner *et al.*, “Tribological performance of titanium samples oxidized by fs-laser radiation, thermal heating, or electrochemical anodization,” *Appl. Phys. A Mater. Sci. Process.*, vol. 124, no. 4, p. 0, 2018.

[40] D. Zhang, F. Gao, X. Wei, G. Liu, M. Hua, and P. Li, “Fabrication of textured composite surface and its tribological properties under starved lubrication and dry sliding conditions,” *Surf.*

Coatings Technol., vol. 350, no. January, pp. 313–322, 2018.

[41] J. Bonse, S. Hohm, S. V Kirner, A. Rosenfeld, and J. Kruger, “Laser-Induced Periodic Surface Structures-A Scientific Evergreen,” *IEEE J. Sel. Top. Quantum Electron.*, vol. 23, no. 3, 2017.

[42] J. Bonse, “Femtosecond laser micromachining of technical materials,” vol. 4065, pp. 161–172, 2004.

[43] D. Tabor, “Surface effects in adhesion, friction, wear and lubrication,” *Tribology International*, vol. 14, no. 6. pp. 1–631, 1981.

[44] W. Zhai, N. Srikanth, L. B. Kong, and K. Zhou, “Carbon nanomaterials in tribology,” *Carbon N. Y.*, vol. 119, pp. 150–171, 2017.

[45] R. J. Yeo, “Ultrathin Carbon-Based Overcoats for Extremely High Density Magnetic Recording.” pp. 1–167, 2017.

[46] M. Berger and M. Seifert, “Nanotechnology. The Future is Tiny.,” *Angewandte Chemie International Edition*, vol. 56, no. 26. pp. 1–359, 2017.

[47] M. A. • N. A. W. I. M. • C. S. Ozkan and S. M. • J. L. Gervasoni, *GRAPHENE SCIENCE HANDBOOK, Applications and Industrialization*. 2016.

[48] M. J. Nine, M. A. Cole, D. N. H. Tran, and D. Losic, “Graphene: A multipurpose material for protective coatings,” *J. Mater. Chem. A*, vol. 3, no. 24, pp. 12580–12602, 2015.

[49] N. Kumar, R. T. Ginting, and J. W. Kang, “Flexible, large-area, all-solid-state supercapacitors using spray deposited PEDOT:PSS/reduced-graphene oxide,” *Electrochim. Acta*, vol. 270, pp. 37–47, 2018.

[50] C. E. Walker, Z. Xia, Z. S. Foster, B. J. Lutz, and Z. H. Fan, “Investigation of airbrushing for fabricating microelectrodes in microfluidic devices,” *Electroanalysis*, vol. 20, no. 6, pp. 663–670, 2008.

[51] A. F. M. Ibrahim and Y. S. Lin, “Synthesis of graphene oxide membranes on polyester substrate by spray coating for gas separation,” *Chem. Eng. Sci.*, vol. 190, pp. 312–319, 2018.

[52] “PEGASUS - Plasma Enabled and Graphene Allowed Synthesis of Unique nanoStructures.” [Online]. Available: https://www.ipfn.tecnico.ulisboa.pt/PEGASUS/.

[53] Y. Liu, J. Zhang, S. Li, Y. Wang, Z. Han, and L. Ren, “Fabrication of a superhydrophobic graphene surface with excellent mechanical abrasion and corrosion resistance on an aluminum alloy substrate,” *RSC Adv.*, vol. 4, no. 85, pp. 45389–45396, 2014.

[54] F. Guo *et al.*, “Graphene-based environmental barriers,” *Environ. Sci. Technol.*, vol. 46, no. 14, pp. 7717–7724, 2012.

[55] H. Liang, Y. Bu, J. Zhang, Z. Cao, and A. Liang, “Graphene oxide film as solid lubricant,” *ACS*

Appl. Mater. Interfaces, vol. 5, no. 13, pp. 6369–6375, 2013.

[56] D. Berman, A. Erdemir, and A. V Sumant, “Few layer graphene to reduce wear and friction on sliding steel surfaces,” *Carbon N. Y.*, vol. 54, pp. 454–459, 2013.

[57] D. Berman, A. Erdemir, and A. V Sumant, “Reduced wear and friction enabled by graphene layers on sliding steel surfaces in dry nitrogen,” *Carbon N. Y.*, vol. 59, pp. 167–175, 2013.

[58] D. Zheng, Z. bing Cai, M. xue Shen, Z. yang Li, and M. hao Zhu, “Investigation of the tribology behaviour of the graphene nanosheets as oil additives on textured alloy cast iron surface,” *Appl. Surf. Sci.*, vol. 387, pp. 66–75, 2016.

[59] Y. Wei, Y. Zhang, X. Gao, Y. Yuan, B. Su, and C. Gao, “Declining flux and narrowing nanochannels under wrinkles of compacted graphene oxide nanofiltration membranes,” *Carbon N. Y.*, vol. 108, pp. 568–575, 2016.

[60] N. A. Ismail and S. Bagheri, “Highly oil-dispersed functionalized reduced graphene oxide nanosheets as lube oil friction modifier,” *Mater. Sci. Eng. B Solid-State Mater. Adv. Technol.*, vol. 222, pp. 34–42, 2017.

[61] L. Liu *et al.*, “Recent advances in friction and lubrication of graphene and other 2D materials: Mechanisms and applications,” *Friction*, vol. 7, no. 3, pp. 199–216, 2019.

[62] H. Xie *et al.*, “Tribological behaviors of graphene and graphene oxide as water-based lubricant additives for magnesium alloy/steel contacts,” *Materials (Basel).*, vol. 11, no. 2, pp. 1–17, 2018.

[63] A. Carapeto, “Estudo de dois novos DLC ’ s para revestimento de próteses articulares : Efeito da albumina no seu comportamento tribológico.” pp. 1–81, 2009.